ISSN 2657-6260

2020 (LXI)
Vol. 223, No. 4

SCIENTIFIC JOURNAL OF POLISH NAVAL ACADEMY

Formerly ZESZYTY NAUKOWE AKADEMII MARYNARKI WOJENNEJ

Gdynia 2020

All articles in the quarterly have been peer reviewed

The original (reference) version of the journal is the online version

Abstracting & Indexing

Arianta
Baidu Scholar
BazTech
CEON Biblioteka Nauki
CNKI Scholar (China National Knowledge Infrastructure)
CNPIEC
Dimensions
DOAJ
EBSCO Discovery Service
Google Scholar
Index Copernicus
J-Gate
KESLI-NDSL (Korean National Discovery for Science Leaders)
Naviga (Softweco)
POL-index
Primo Central (ExLibris)
ReadCube
Summon (Serials Solutions/ProQuest)
TDNet
WorldCat (OCLC)

Website quarterly
https://content.sciendo.com/view/journals/sjpna/sjpna-overview.xml
https://www.amw.gdynia.pl/index.php/nauka/czasopisma-naukowe/item/45-zeszyty-naukowe

Journal Owner and Publisher
Akademia Marynarki Wojennej/Polish Naval Academy

Contact
Redakcja Zeszytów Naukowych AMW
Akademia Marynarki Wojennej
Inż. J. Śmidowicza 69, 81-127 Gdynia
tel. 261 26 29 72
e-mail: b.rozanska@amw.gdynia.pl; wydawnictwo@amw.gdynia.pl

CONTENTS

SCIENTIFIC JOURNAL OF POLISH NAVAL ACADEMY
2020(LXI) 4(223)

sciendo

DOI: 10.2478/sjpna-2020-0012

DOPPLER EFFECT IN 2×2 TO 4×4 MIMO SYSTEMS OF WIRELESS COMMUNICATION WITH ORTHOGONAL PILOT CHANNEL ESTIMATION

Vadim Romanuke*

**Polish Naval Academy, Faculty of Mechanical and Electrical Engineering, Śmidowicza 69 Str., 81-127 Gdynia, Poland; e-mail: v.romanuke@amw.gdynia.pl; ORCID ID: 0000-0003-3543-3087*

ABSTRACT

The Doppler effect in 2×2, 3×3, 4×4 MIMO wireless communication systems with channel estimation is studied. The orthogonal pilot signal approach is used for the channel estimation, where the Hadamard sequences are used for piloting, along with the eight alternative orthogonal sets similar to the Walsh set. MIMO transmissions are simulated for 10 cases of the frame length and pilot symbols per frame by no Doppler shift to 1100 Hz Doppler shift with a step of 100 Hz. Based on the simulation, it is ascertained that MIMO transmissions of shorter frames are less sensitive to the Doppler effect. Despite increasing the number of antennas does not mitigate the Doppler effect, and the bit-error rate performance of 4×4 MIMO systems worsens faster than that of 2×2 MIMO systems, it is better to use the maximum number of antennas. The Doppler effect does badly worsen the performance at highway and express train speeds (100 km/hr, and faster), leaving only possibility to further shorten transmissions. This, however, decreases the data rate, but the respective accuracy-versus-data-rate tradeoff must be acceptable.

Key words:
wireless communication, MIMO, Doppler effect, transmit-receive antenna pairs, bit-error rate.

Research article

INTRODUCTION

As of 2020, the 5G wireless communication technology is still being embedded, where the MIMO technique is extensively used for multiplying the capacity of a radio link by using multiple antennas at the transmitter and receiver ends [1]. Where possible, massive MIMO systems are being implemented, but MIMO systems with just a few transmit-receive antenna pairs are believed to be still used at least for a decade.

To sustain high quality of links under combined effects of scattering, fading, and power decay with distance, MIMO operates on channel state information (CSI) [1, 3, 10]. The CSI is extracted from the received signal by using orthogonal pilot signals prepended to every packet [4]. If the CSI is based only on the received data, without any known transmitted sequence (which is called a blind approach), the tradeoff is the accuracy versus the overhead. Thus, the orthogonal pilot signal approach (OPSA) has a higher overhead, but it achieves a better channel estimation accuracy than the blind approach [15].

It is well known that the quality of wireless communication may worsen when either the transmitter or receiver end is in motion (or they both are). This occurs due to the Doppler effect [5, 9]. Obviously, influence of Doppler shifts on the MIMO performance at human-walking speeds is negligible. At vehicular speeds, however, the influence is experienced to be significant even by using CSI with OPSA. In particular, the data rate may dramatically decrease as the vehicle starts accelerating and keeps moving further at least at urban speeds, let alone highway speeds [9, 12].

MOTIVATION AND GOAL

An end-to-end MIMO system is successfully simulated by using a random data generator, modulator [12], the orthogonal space-time block coding (OSTBC) technique [2, 11], fading channel models with additive white Gaussian noise [5], an OSTBC combiner [2], and a demodulator [3, 10]. These blocks are connected successively. The CSI with OPSA is commonly realized by orthogonal codes taken from the Hadamard matrix [12], where the first orthogonal sequence of pilot symbols is the sequence of ones. This sequence is the Walsh function of the zeroth order, which is a function-constant [13]. In particular, Walsh functions are generated from

the Hadamard matrix [14], and can be used as well for other transmit antennas. Another possibility is to use alternative orthogonal sets similar to the Walsh set [6].

Whereas MIMO systems ensure high data rates and power efficiency, an open question is how indeed the Doppler effect influences the MIMO system with a few transmit-receive antenna pairs. Therefore, the goal is to estimate the bit-error rate (BER) performance of 2×2, 3×3, and 4×4 MIMO systems using CSI with OPSA for a wide range of Doppler shifts. For this, along with Walsh codes, alternative orthogonal sets in the OPSA are to be tried as well [6, 7], and various relationships of the frame length and pilot symbols per frame will be considered. The estimated BER performance is believed to answer the question by ascertaining whether increasing the number of antennas mitigates the Doppler effect. If the Doppler effect does badly worsen the BER performance, the respective breaking points or ranges should be described. Eventually, a possibility of using CSI with OPSA by more appropriate orthogonal sets is to be studied as well.

SET-UP AND PARAMETERS OF THE SIMULATION

The set-up and simulation are based on MATLAB® R2019a Communications System Toolbox™ functions covering end-to-end MIMO systems which employ a few transmit and a few receive antennas. The random data are taken as pseudorandom integers drawn from the discrete uniform distribution on the interval from 0 to $M-1$, where M is the number of transmit-receive antenna pairs. For using 2 to 4 transmit antennas, the signal is modulated by applying the quaternary phase shift keying (QPSK) method. The modulated signal is then encoded by using the OSTBC technique. The input symbols are mapped block-wise, and the output codeword matrices are concatenated in the time domain. It is worth noting that the symbol rate of the code is 1 for a 2×2 MIMO system, and 3/4 for 3×3 and 4×4 MIMO systems.

The frame length denoted by F is set at 36, 72, 144, 288 symbols. The number of pilot symbols per frame denoted by P cannot exceed 25 % of the frame length, so it is set according to tab. 1, with respect to each frame length. In an M×M MIMO system, the M pilot sequences of P-positioned codes are taken as the first M Walsh Hadamard-ordered functions from the basis of P functions. Alternatively, the M pilot sequences of P-positioned codes are taken as the last M functions from each of the eight orthogonal bases of P partially unsymmetrical binary functions [6, 8].

Tab. 1. The 10 cases of the frame length and pilot symbols per frame

F	**36**	**72**	**144**	**288**	**frame length**
P	8	8	8	8	number of pilot symbols per frame
	P	16	16	16	
		P	32	32	
			P	64	

The modulated and encoded data are transmitted through flat-fading Rayleigh channels [12], to which white Gaussian noise is added. Each frame is passed by a ratio of bit energy to noise power spectral density. The ratio denoted by $r_{\mathrm{Eb/No}}$ is measured in dB. The range of $r_{\mathrm{Eb/No}}$ is set from 0 dB to 8 dB with a step of 1 dB. Besides, it is assumed that the channel remains unchanged for the length of the packet (i. e., it undergoes slow fading), and the channel undergoes independent fading between the multiple transmit-receive antenna pairs [1, 12]. The number of errors cannot exceed 10 % of the number of packets, so the maximum number of errors is set at 5000, whereas the maximum number of packets is set at 50000. This number is believed to be sufficient for obtaining statistically stable (i. e., reliable) results of the simulation.

At the receiving end, the signals from all of the receive antennas and the channel estimate signal are combined to extract the soft information of the symbols encoded by the OSTBC. The combining algorithm uses only the estimate for the first symbol period per codeword block. The output of the combiner is demodulated using the QPSK method. Finally, the BER is estimated and fitted to a curve.

RESULTS OF THE SIMULATION

For each of those 10 cases in tab. 1, the BER is plotted versus $r_{\mathrm{Eb/No}}$ with squared points for Hadamard sequences, and with circled points for the other orthogonal sequences from each of the eight above-mentioned orthogonal bases. The BER performance by no Doppler shift is shown in fig. 1. The polylines for 2×2 MIMO systems are above the polylines for 3×3 MIMO, and the latter are above the polylines for 4×4 MIMO. This order remains the same for the polylines of the BER by 100 Hz Doppler shift (fig. 2). The 200 Hz Doppler shift (fig. 3) and 300 Hz Doppler shift (fig. 4) also seem to have no significant influence on the BER performance.

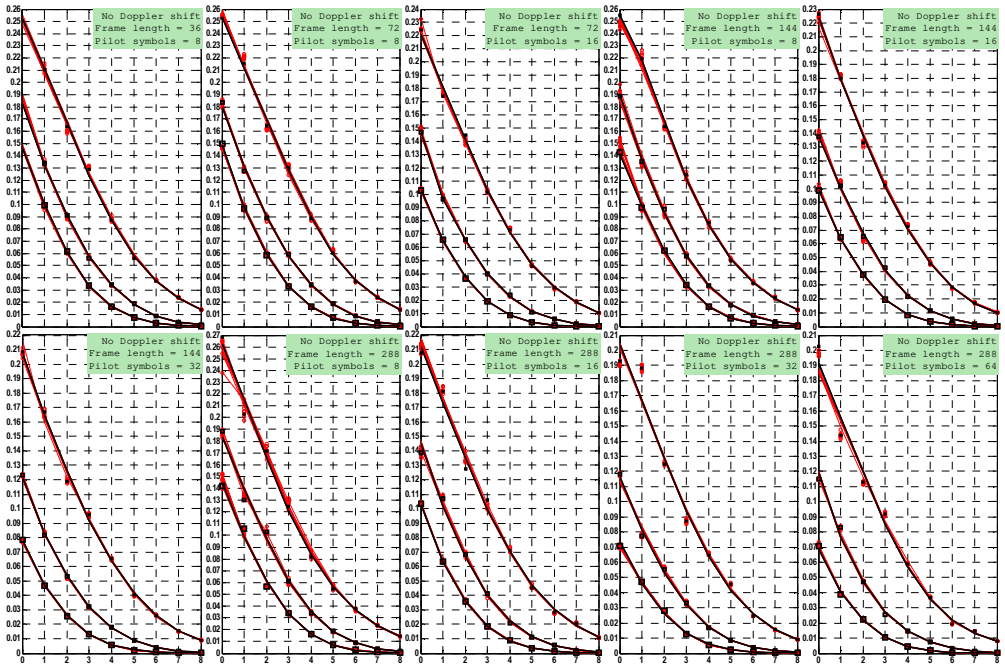

Fig. 1. The BER performance by no Doppler shift

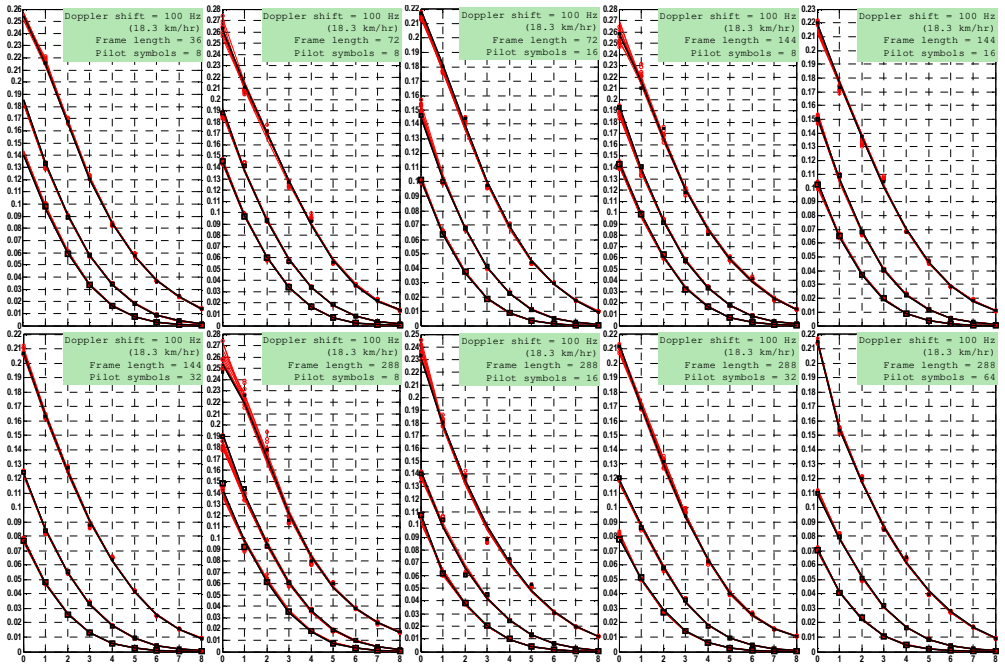

Fig. 2. The BER performance by 100 Hz Doppler shift

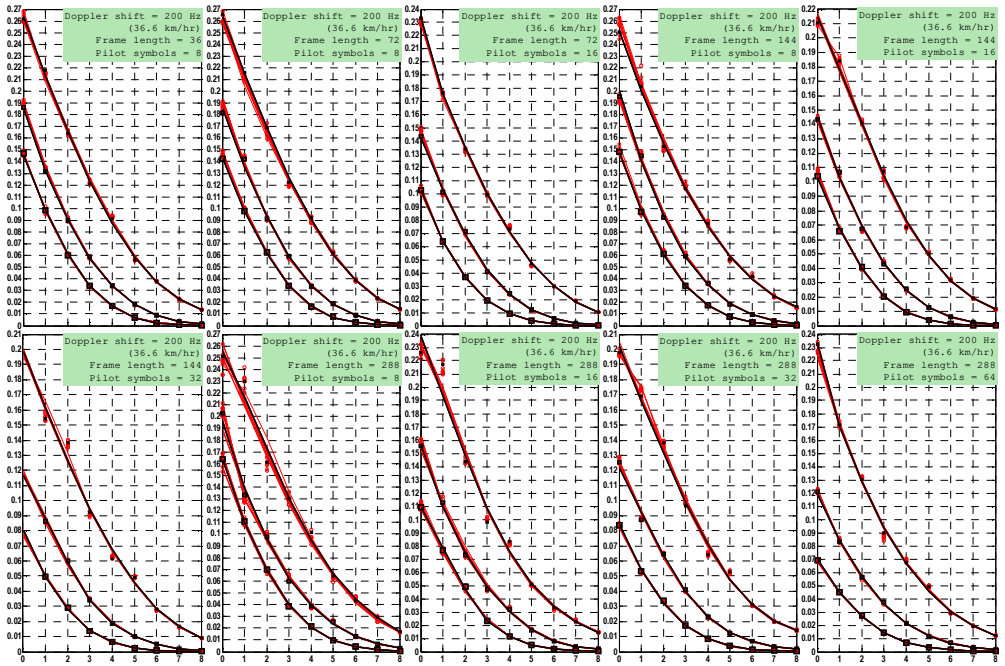

Fig. 3. The BER performance by 200 Hz Doppler shift

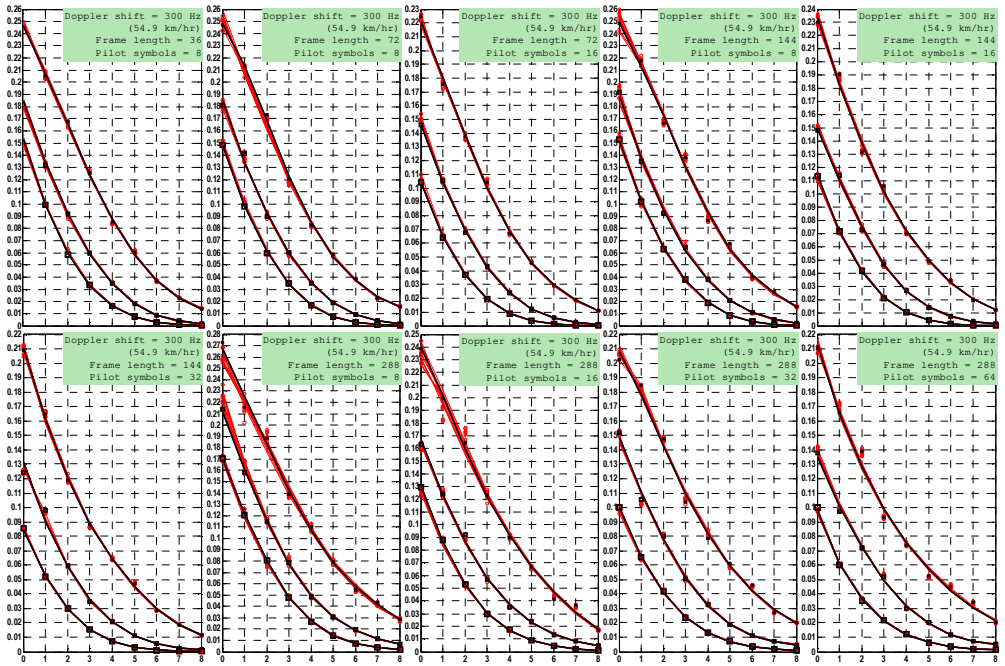

Fig. 4. The BER performance by 300 Hz Doppler shift

However, if to study the polylines in detail, the BER worsening is noticeable for the four following cases of the frame length and pilot symbols per frame:

$$\{F=288, P=8\},\ \{F=288, P=16\},\ \{F=288, P=32\},\ \{F=288, P=64\}. \quad (1)$$

Thus, even at urban speeds close to 60 km/hr, the long-framed 2×2 to 4×4 MIMO transmissions become slightly prone to the Doppler effect. Besides, the BER performance by

$$\{F=144, P=32\} \quad (2)$$

at such speeds for 3×3 and 4×4 MIMO systems (see fig. 3 and fig. 4) seems to be better than that by

$$\{F=288, P=64\}, \quad (3)$$

although the BER performance by (3) without motion (by no Doppler shift) is the best (see fig. 1).

Nevertheless, the BER here does not badly increase. It is worth to note that the speed ($\tilde{v}$) is estimated approximately by assuming that the carrier frequency is 5.9 GHz, whereas the general relationship is [9]

$$\tilde{v}=\frac{1.08\cdot S_{\text{Doppler}}}{f_{\text{carrier}}} \quad (4)$$

for a Doppler shift S_{Doppler} in Hz and a carrier frequency f_{carrier} in GHz. So, lesser carrier frequencies correspond to faster motion. For instance, the speed by $f_{\text{carrier}}=2.4$ GHz and 300 Hz Doppler shift is 135 km/hr, which is rather highway speed. The BER worsening for the cases of (1) at highway speeds cannot be reckoned noticeable.

At the Doppler shift of 400 Hz (fig. 5), it is especially noticeable that the BER of 4×4 MIMO at $r_{\text{Eb/No}}=8$ dB for the cases of (1) becomes worse than that at $S_{\text{Doppler}}=300$ Hz (fig. 4). The worsening builds up at $S_{\text{Doppler}}=500$ Hz (fig. 6), which is quite obvious for 2×2 to 4×4 MIMO polylines for (1), and for

$$\{F=144, P=8\},\ \{F=144, P=16\} \quad (5)$$

as well. The Doppler shift of 600 Hz (fig. 7) already corresponds to a highway speed, at which polylines for (1) further distort. Their distortion in fig. 8 is such

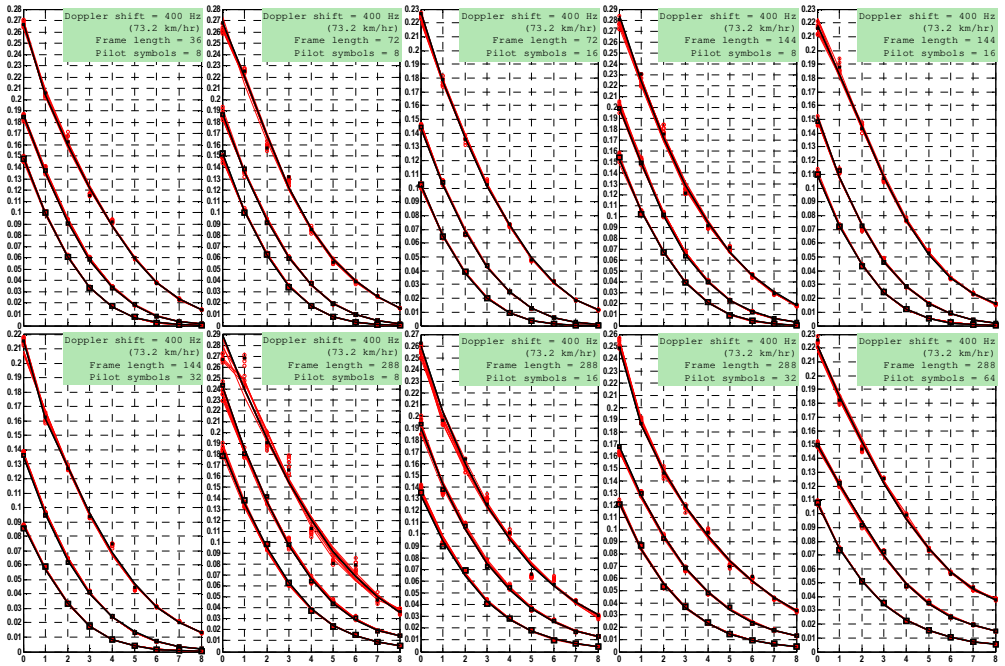

Fig. 5. The BER performance by 400 Hz Doppler shift

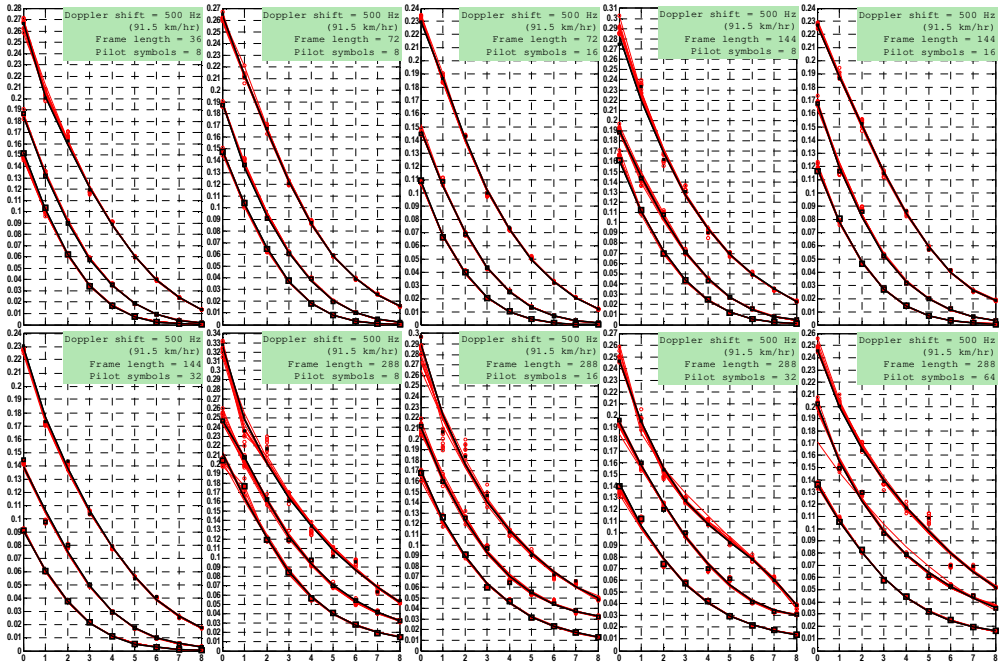

Fig. 6. The BER performance by 500 Hz Doppler shift

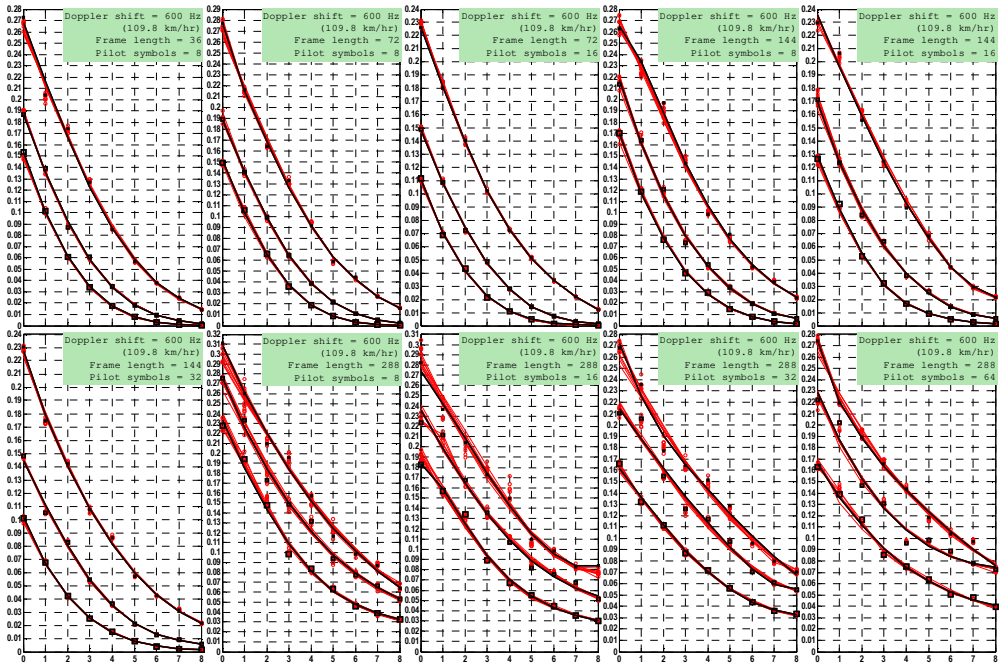

Fig. 7. The BER performance by 600 Hz Doppler shift

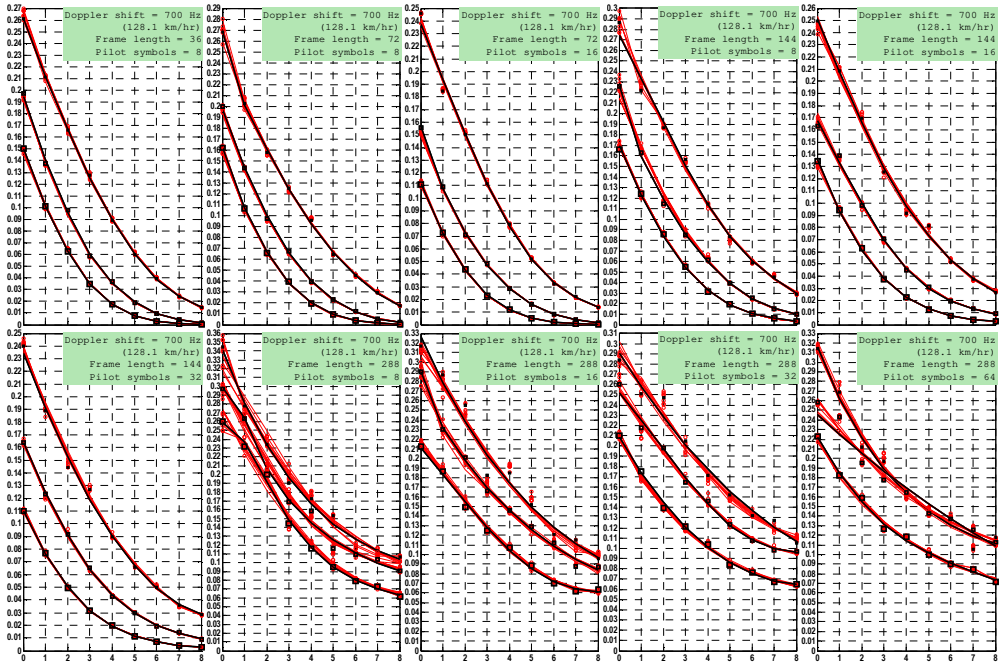

Fig. 8. The BER performance by 700 Hz Doppler shift

that the BER even at $r_{\text{Eb/No}} = 8$ dB for 4×4 MIMO is not less than 0.06, whereas the BER in the remaining six cases (see tab. 1) for 4×4 MIMO is still close to 0 at $r_{\text{Eb/No}} = 8$ dB.

It is obvious that, as the Doppler shift increases from 300 to 700 Hz (the speed increases from urban to highway), the BER performance by (2), i. e. by the medium-framed 2×2 to 4×4 MIMO transmissions, worsens significantly. Indeed, compared to the case without motion (by no Doppler shift), the BER at $r_{\text{Eb/No}} = 8$ dB for 2×2 MIMO has increased from 0.01 to 0.03, although the BER at $r_{\text{Eb/No}} = 0$ dB for 2×2 MIMO has increased from 0.21 to 0.24 (just about 14 %). The other medium-framed MIMO transmissions by (5) have "suffered" also, especially 3×3 and 4×4 MIMO at the Doppler shift of 600 Hz (fig. 7), where the motion speed exceeds 100 km/hr.

It is worth noting that short-framed 2×2 to 4×4 MIMO transmissions by

$$\{F = 32, P = 8\} \tag{6}$$

do not "feel" even the Doppler shift of 700 Hz (fig. 8). At the same time, their performance is still worse than that of MIMO transmissions by (2). However, the performance by (2) at this shift is almost equivalent to the performance by

$$\{F = 72, P = 16\}. \tag{7}$$

As the Doppler shift further increases (fig. 9 – 12), the polylines for long-framed 2×2 to 4×4 MIMO transmissions by (1) further exfoliate. The polylines for medium-framed 2×2 to 4×4 MIMO transmissions by (5) and (2) do not seem exfoliated, but their BER performance becomes visibly worse. The performance by

$$\{F = 72, P = 8\} \tag{8}$$

and (7) worsens also, but the respective polylines are not seen badly exfoliated even at $S_{\text{Doppler}} = 1100$ Hz (fig. 12), which corresponds to over 200 km/hr.

Amazingly enough, short-framed 3×3 and 4×4 MIMO transmissions by (6) are not influenced by the Doppler effect at highway and express train speeds. Indeed, the respective polylines in fig. 1 and fig. 12 are almost the same. However, the best BER performance at such speeds is produced by (7), where the BER at $r_{\text{Eb/No}} = 0$ dB for 4×4 MIMO is about 0.12, which is comparable to the averaged BER performance at urban speeds (see fig. 13 and its subplot for $S_{\text{Doppler}} = 300$ Hz).

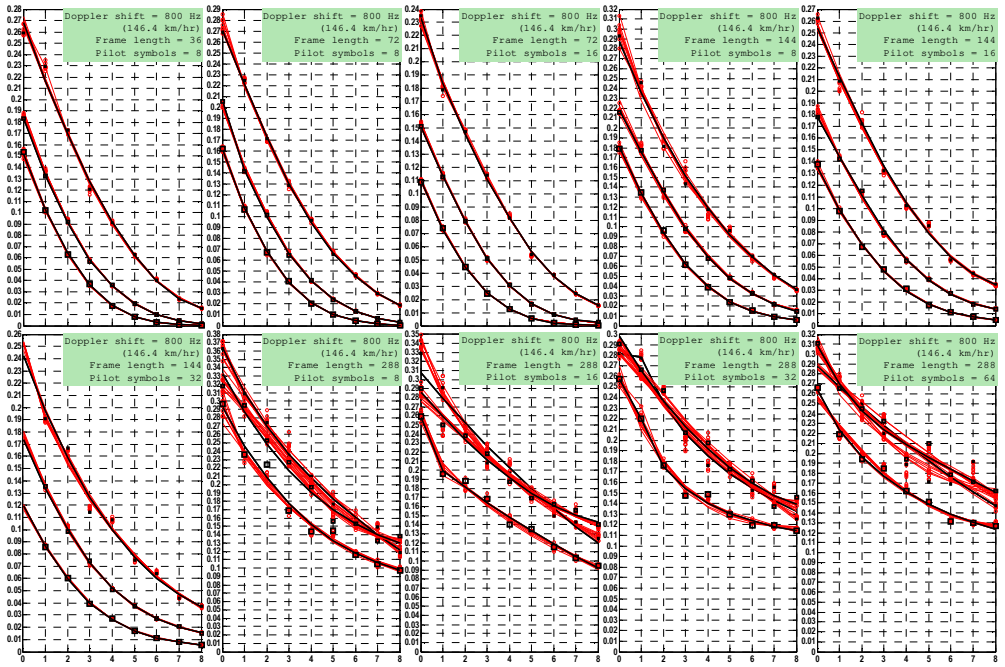

Fig. 9. The BER performance by 800 Hz Doppler shift

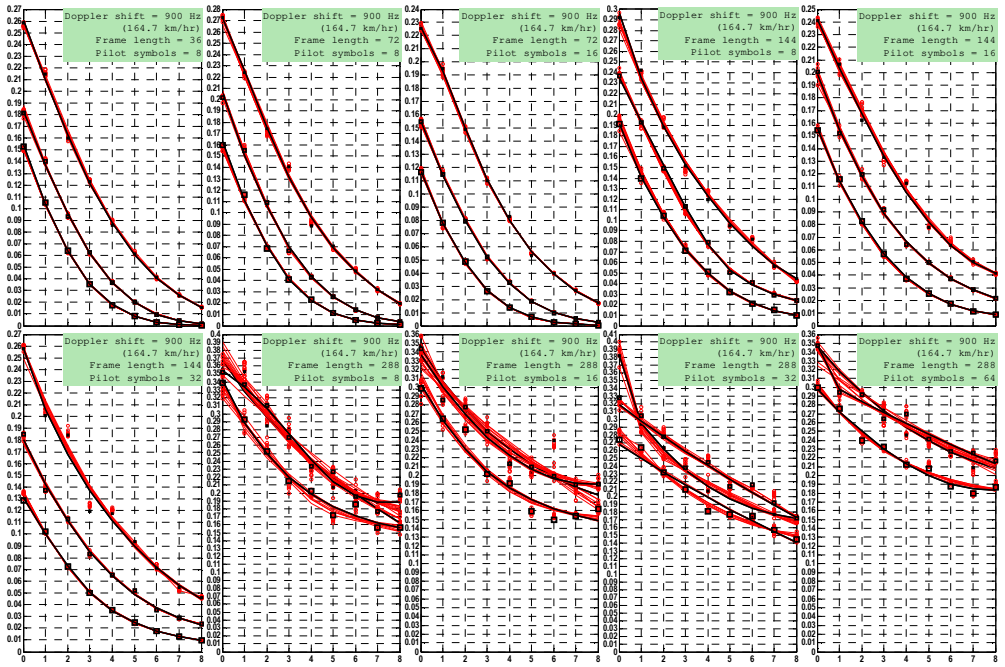

Fig. 10. The BER performance by 900 Hz Doppler shift

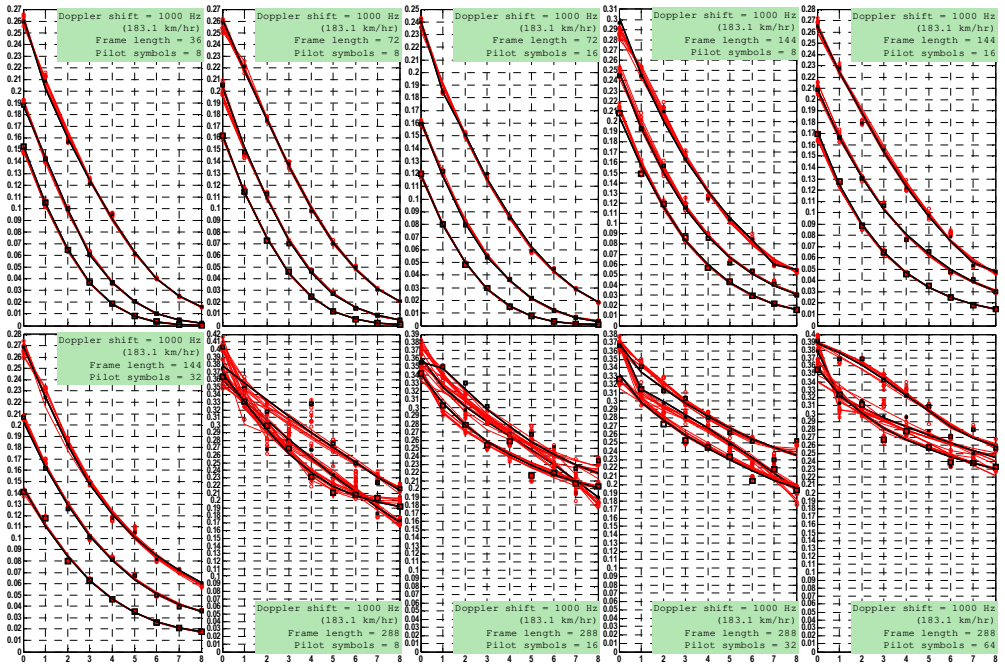

Fig. 11. The BER performance by 1000 Hz Doppler shift

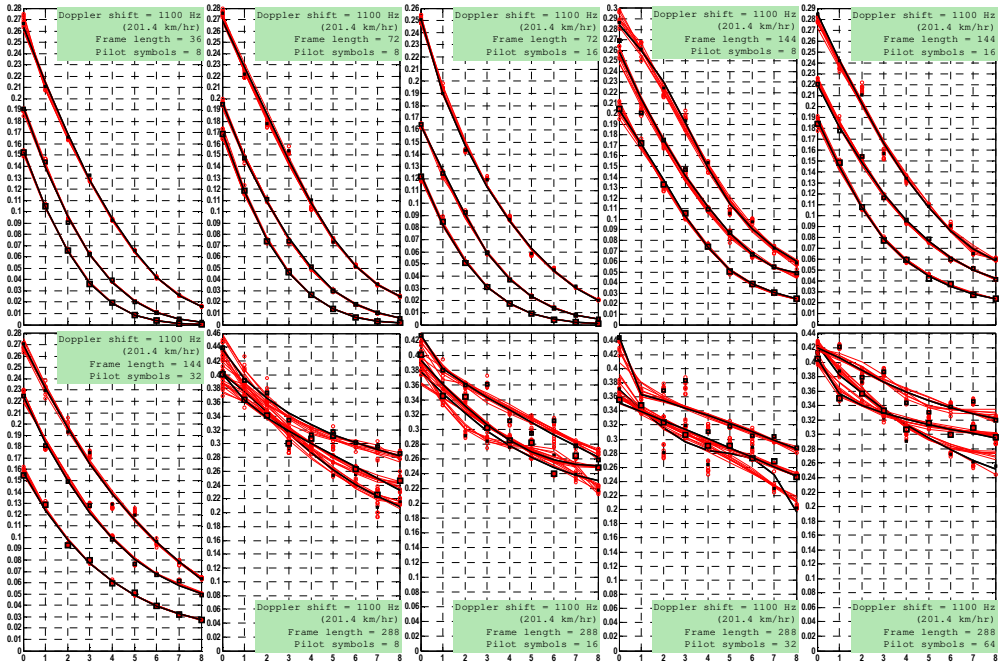

Fig. 12. The BER performance by 1100 Hz Doppler shift

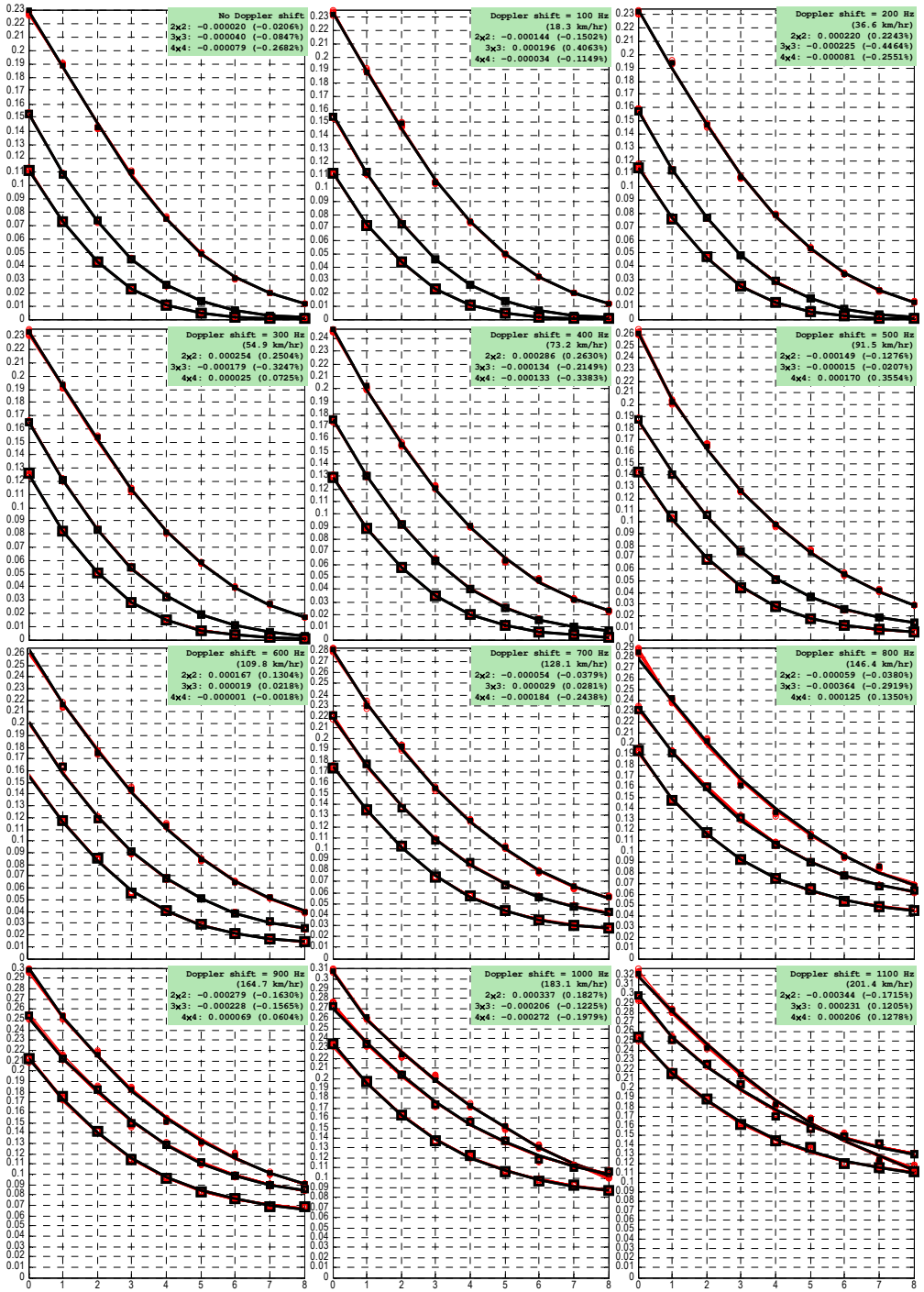

Fig. 13. The averaged BER performance by no Doppler shift to 1100 Hz Doppler shift

DISCUSSION

The polylines in fig. 1 – 12 allow to see that the BER badly increases for MIMO transmissions of longer frames. In other words, the shorter the frame is, the less sensitive to the Doppler effect the MIMO system will be. Such sensitivity is clearly seen from the analysis of the respective polylines in fig. 1 – 12, which do have observable differences (their resemblance is delusive). Meanwhile, increasing the number of antennas does not mitigate the Doppler effect. Although the MIMO system with the greater number of transmit-receive antenna pairs has strictly better performance (up at urban and highway speeds), the BER of 4×4 MIMO systems worsens faster than that of 2×2 MIMO systems. For instance, at $r_{\mathrm{Eb/No}} = 0$ dB for 2×2 MIMO, the averaged BER increases from 0.23 (by no Doppler shift) to 0.3 (by 900 Hz Doppler shift), whereas it increases from 0.11 (by no Doppler shift) to 0.21 (by 900 Hz Doppler shift) for 4×4 MIMO (see fig. 13). In relative units, the performance decrement here is 30.4 % for 2×2 MIMO versus 90.9 % for 4×4 MIMO.

The 12 subplots in fig. 13 contain differences (in absolute units and percentage) between the averaged BER performance by the Hadamard sequences and partially unsymmetrical binary sequences [6, 8]. The differences are quite small (less than 0.5 %), and so they are insignificant. This implies that using CSI with OPSA by Hadamard sequences in 2×2 to 4×4 MIMO systems cannot be improved.

CONCLUSIONS

The Doppler effect starts worsening the BER performance of 2×2 to 4×4 MIMO systems using CSI with OPSA at urban speeds close to 60 km/hr, and faster. This can be prevented by shortening the frame length (along with the respective length of pilot sequence). Despite increasing the number of antennas does not mitigate the Doppler effect, and the BER of 4×4 MIMO systems worsens faster than that of 2×2 MIMO systems, it is better to use the maximum number of antennas (by simultaneously shortening the frame length). At highway and express train speeds (100 km/hr and faster), it is impossible to use long-framed 2×2 to 4×4 MIMO transmissions, whichever the pilot sequence length is. The Doppler effect does badly worsen the BER performance at such speed ranges, leaving only possibility to further shorten transmissions (and thus decreasing the data rate). The respective accuracy-versus-data-rate tradeoff herein must be acceptable.

Using CSI with OPSA by orthogonal sequences similar to Hadamard sequences is possible but it does not improve the BER performance of MIMO systems against the Doppler effect. Nonetheless, the cases of the frame length and pilot symbols per frame and the range of Doppler shifts have been studied under presumption of the perfect orthogonality of pilot sequences. Surely, a de-orthogonalization in pilot sequences by using CSI with OPSA is not excluded, so this special case should be considered in a further research.

REFERENCES

[1] Berger L. T., Schwager A., Pagani P., Schneider D. M., *MIMO Power Line Communications: Narrow and Broadband Standards, EMC, and Advanced Processing. Devices, Circuits, and Systems*, CRC Press, 2014.

[2] Larsson E., Stoica P., *Space-Time Block Coding For Wireless Communications*, Cambridge University Press, UK, 2003.

[3] Lee W. C. Y., *Mobile Communications Engineering: Theory and Applications*, 2nd Ed., McGraw-Hill, 1998.

[4] Naguib A. F., Tarokh V., Seshadri N., Calderbank A. R., *Space-time codes for high data rate wireless communication: Mismatch analysis*, Proceedings of IEEE International Conference on Communications, Montréal, Québec, Canada, 8–12 June 1997, pp. 309–313.

[5] Pätzold M., *Mobile Fading Channels*, Wiley, 2002.

[6] Romanuke V. V., *Computational method of building orthogonal binary functions bases for multichannel communication systems with code channels division*, Mathematical Modeling and Computational Methods, Ternopil State Technical University, Ternopil, Ukraine, 2006.

[7] Romanuke V. V., *Generalization of the eight known orthonormal bases of binary functions to the eight orthonormal bases of binary surfaces*, 'Optoelectronic Information-Power Technologies', 2007, No. 2, pp. 263–271.

[8] Romanuke V. V., *Simulation of code division by applying systems of orthogonal binary functions* $\{\mathrm{wal}(w,\theta)\}_{w=0}^{L-1}$ *and* $\left\{\{\mathrm{rom}_u(r,\theta)\}_{r=0}^{L-1}\right\}_{u=1}^{8}$ *in L-channeled CDMA-system*, 'Herald of Khmelnytskyi National University. Technical sciences', 2008, No. 6, pp. 121–132.

[9] Skolnik M., *Introduction to Radar Systems*, 3rd Ed., McGraw-Hill, New York, 2001.

[10] Stern H., Mahmoud S., *Communications Systems*, Pearson Prentice Hall, 2004.

[11] Tarokh V., Jafarkhami H., Calderbank A. R., *Space-time block codes from orthogonal designs*, 'IEEE Transactions on Information Theory', 1999, Vol. 45, No. 5, pp. 1456–1467.

[12] Tsoulos G., *MIMO System Technology for Wireless Communications*, CRC Press, 2006.

[13] Walsh J. L. *A closed set of normal orthogonal functions*, 'American Journal of Mathematics', 1923, Vol. 45, No. 1, pp. 5–24.

[14] Zhihua L., Qishan Z., *Ordering of Walsh Functions*, 'IEEE Transactions on Electromagnetic Compatibility', 1983, Vol. EMC-25, No. 2, pp. 115–119.

[15] Zhuang A., Lohan E. S., Renfors M., *Comparison of decision-directed and pilot-aided algorithms for complex channel tap estimation in downlink WCDMA systems*, Proceedings of 11th IEEE Personal and Indoor Mobile Radio Communications (PIMRC), Vol. 2, London, UK, September 2000, pp. 1121–1125.

EFEKT DOPPLERA W SYSTEMACH KOMUNIKACJI BEZPRZEWODOWEJ OD 2×2 DO 4×4 MIMO Z OSZACOWANIEM KANAŁU PRZEZ PILOTA ORTOGONALNEGO

STRESZCZENIE

W pracy przedstawiono badania efektu Dopplera w systemach komunikacji bezprzewodowej 2×2, 3×3, 4×4 MIMO z estymacją kanału. W procesie szacowania kanału zastosowano podejście sygnału pilotującego w wykorzystaniem sekwencji Hadamarda, wraz z ośmioma alternatywnymi zestawami baz ortogonalnych, podobnymi do zestawu Walsha. Transmisje MIMO zostały zasymulowane dla 10 przypadków, różniących się długością ramki i symboli pilotujących oraz częstotliwością Dopplera, której zakres zmieniał się od 0 do 1100 Hz z krokiem 100 Hz. Na podstawie badań symulacyjnych wykazano, że transmisje krótszych ramek MIMO są mniej wrażliwe na efekt Dopplera. Pomimo, że zwiększenie liczby anten nie zmniejsza efektu Dopplera, a wydajność współczynnika błędnych bitów w systemach 4×4 MIMO pogarsza się szybciej niż w systemach 2×2 MIMO, przeprowadzone badania wskazują na korzyści z zastosowania większej ilości anten. Efekt Dopplera znacznie pogarsza jakość transmisji przy prędkościach powyżej 100 km/h (ruch samochodów na autostradach lub pociągów ekspresowych), determinując potrzebę redukcji przesyłanych danych. To jednak zmniejsza szybkość transmisji danych, ale odpowiedni kompromis między dokładnością a szybkością przesyłania danych musi być akceptowalny.

Słowa kluczowe:

komunikacja bezprzewodowa, MIMO, efekt Dopplera, pary anten nadawczo-odbiorczych, współczynnik błędnych bitów.

SCIENTIFIC JOURNAL OF POLISH NAVAL ACADEMY
2020 (LXI) 4 (223)

sciendo

DOI:10.2478/sjpna-2020-0013

POSSIBILITIES OF DETECTION OF THE JAMMING OF THE GNSS RECEIVER WITH THE HELICAL ANTENNA

Andrzej Felski[1] Piotr Stopienski[2*]

[*] *Polish Naval Academy, Faculty of Navigation and Naval Weapons, Śmidowicza 69 Str., 81-127 Gdynia, Poland; [1]e-mail: a.felski@amw.gdynia.pl; [1]ORCID ID: 0000-0002-0326-3397; [2]e-mail: p.stopienski@o2.pl*

ABSTRACT

Jamming of GNSS signals is lately treated as essential threat for GNSS users. It is especially dangerous in the face of common usage of GPS-like systems in everyday life, and the great belief of everyday users in the truth of devices indications. In spite of the legal prohibition of using them, jammers are commonly accessible, especially in the Internet. Last years showed however that such threat generated purposely also some governments, what is clearly visible in armed conflicts, and during military exercises. Of course this creates the great threat for civilian users if will be in the vicinity.

Applications and services based upon GNSS are becoming increasingly embedded in modern society, so community have now become critically dependent upon their correct operation. This refers positioning first of all, but telecommunications networks, power grids, financial transactions, whole world of logistics are dependant as well. The main users of GNSS, both professional and non-professional smartphones users are not prepared on such situation, and usually have no technical possibilities to detect of jamming. For operators of critical installations, for example seaports, or airfields, the detection of jamming cases is extremely important. It can be provided with special devices, which are usually based on specific antennas, and deep analysis of signal. In this paper experiments in detection of the jamming with helical antennas are discussed

Keywords:
GNSS Receiver, helical antenna.

Research article

INTRODUCTION

Global Navigation Satellite System (GNSS) is a common acronym for US Global Positioning System (GPS), and similar to them: Russian GLONASS, European Union Galileo, and BeiDou of China. There are accessible for free, and widely used in many fields, including navigation, positioning, surveillance, search and rescue, as well as in many field based on precise timing (electric power net, banking, communication etc.), and other public services (for example such applications as tracking of costly goods, pay-as-you-drive services, sport application, even wild animals behavior monitoring). However the weak side of all these systems is the low power of radio-transmitters installed on satellites, so signal received on the Earth is very week. Their vulnerability to radio frequency interference (RFI) is drawing significant attention, as it is especially problematic for GNSS-based safety-of-life services, such as aviation, or digital mobile communication. Complete list of possible sources of GNSS receiver malfunctioning consists[5] of:

- User's receiver and antenna noise,
- Multipath, which is especially important in urban area,
- Atmosphere status, in which solar activity, and its influence on the state of Ionosphere (its ionization) are the most important,
- Space segment errors, mainly orbit perturbation, but even erroneous data, and possible Space Vehicle (SV) faults,
- Cyber-attacks on Ground Segment, or on satellites,
- Unintentional interferences with other radio signals,
- Intentional disturbances in GNSS satellites signals.

Apart from the multipath, only natural disturbances for long time has been discussed as the serious threat for GPS. The special attention was directed on the activity of the Sun, and state of Ionosphere which especially determined the threat for such systems in polar, and magnetic equator areas. But now it is clear, that the main threat for GNSS systems are intentionally produced false signals in GNSS spectrum. In this threat of jamming (the process of generating a radio-waves of noise character in the GPS spectrum to block or interfere with satellite signals) is the most common, but nowadays spoofing is observed in many places also. Spoofing, is a more complicated activity, and puts on thatching itself under satellite of the system, and transmission of false signals whose the receiver will not recognise, and makes receiver believe it is at false location. Jamming is a kind of activity which form a powerful radio signal, intentionally generated to disturb GNSS service. The most popular jammer has power in miliwatt, but there are military jammers with power of dozen of Watt. Depending on power of the jammer, the size of an area where jamming may

appear is from few meters to hundreds kilometers. It is an illegal activity[1], however they appear in our everyday life everywhere. Probably the most known example is the case of Newark International Airport, where truck driver was using the jammer for a long time to counteract monitoring his activity by his boss [20], but his jammer was so powerful, that it was disrupting Ground-Based Augmentation System ground station. Later similar accidents was notified on many airfields.

Another commonly known example of jamming is the activity of North Korea's military forces against South Korea in region of Seoul and Inchon Airport. This events are examples of the problem [17]. Since the engagement of Russia into the conflict in Syria, similar events are every-day-reality in the eastern part of the Mediterranean Sea.

In spite of jamming, last four years accidents of spoofing are observed more often. This is activity in which some false signals similar to GNSS are generated with the aim to deceive user's receiver. As an result the false coordinates will be calculated.

Whether one likes it, or not, our society has become strongly dependent on the Positioning, Navigation, and Timing infrastructure. The widespread of the GNSS use in all aspects of everyday life entails the average user's belief in the truth of data presented by receiver. Today it is clear that our world urgently wants immune and resilient PNT systems [1]. It is not only question about position, or navigation, but many other critical infrastructures of our society would literally collapse in case of a GNSS failure. The transfer of time data is equally essential for GPS service. Without it, data systems, and energy systems cannot work. In this context, the opportunity to detect such events are critical.

JAMMERS

GNSS jamming is a form of intentional radio-interferences generated by devices, which deliberately transmit signals at the specified frequencies with the power sufficient for disrupting GNSS-based services. In this way GNSS-based services can be disrupted on distances up to of several kilometers from jammer, it depends mainly on the power of the jammer. However, the impact of jamming depends also on receiver circuit, antenna characteristics, and a spectrum of signal generated by jammer. Jamming is not the zero-one process: on some distances jamming is ineffective, on shorter distances it degrades signals of some part of visible satellites, and when even closer, it is completely blocking receiver [12]. The reaction of different

[1] For example in Poland this is the order of Ministry of Transport of 3 July 2007.

types of receivers is dissimilar. Besides, in some part it depends on the height of satellites above the horizon, as satellite elevation is correlated in some part with the signal strength. It causes jamming variety of different space vessels. One can also observe correlation between jamming process, and of the antenna parameters [7]. Briefly the reactions of the same receivers with different antennas vary.

In this context one should dedicate the special attention to jamming devices. Several papers have addressed the problem of characterizing the jamming signal. Probably most jammers used in a civil context can broadcast frequency modulated signals, which covers all GNSS band, or can be periodically moved over the band, mostly in tooth-mode [18]. There are jammers which cover not only the L1 band, but sometimes mobile phones frequency too. Depending on the properties of generated radio, waves jammers can be classified in different ways. Rash [16] suggest to divide jammers into three categories:

1. Continuous wave, occupying less than 100 KHz bandwidth;
2. Narrowband jamming occupying more than 1 MHz of bandwidth, but less than, or equal to, the entire 1.023MHz bandwidth of C/A code;
3. Wideband jamming occupying the entire 10.23 MHz bandwidth about L1, or L2.

Different classification with four classes of jammers was proposed by [14], or [11]:

- Class I: CW signals;
- Class II: single saw-tooth chirp signals;
- Class III, multi saw-tooth chirp signals (the device transmits a frequency modulated signal, but its RF evolution is determined by the combination of several saw-tooth functions);
- Class IV, chirp with signal frequency bursts (the device transmits a frequency modulated signal, and frequency bursts are used to enlarge the frequency band affected by the disturbing signal).

It cannot be in doubt, that professionals have at their disposal devices, which possess completely different properties. There is no information about technics which are implemented for generating jamming signal, but it is clear that power of this group of devices is much higher than "personal" one. So called "electronic countermeasure devices" are offered by Allen Vanguard, CAST, Chronos Technology, Novatel, Forsberg etc. This is not only the domain of the activity of the west forces, as Russia announced its electronic warfare systems too, for example the Borisoglebsk-2, Krasukha, Parodist etc. electronic warfare (EW) complexes which compromises of several stations based on a multi-purpose armoured all-terrain vehicle [13]. There are suggestions in the media, that Turkey, Israel, China, and other countries do the same.

As far as "personal devices" usually possess little power measured in milliwatts, then professional devices generate power even to 500 W.

POSSIBILITIES OF JAMMING COUNERMEASURE

Designers of GPS found that the use of the spread spectrum of the signal would assure the resistance on interferences. In that case nobody anticipated needs of the uses in the receiver of the mechanism verifying the occurrence of disturbances. At the moment the standard GNSS receiver is not equipped with any tool for detecting the jamming, and for ordinary users it is difficult to discover such accident. Most often it ascertains disturbances when the receiver freezes indications, while the carrier changes its own position, or coordinates on the display are completely different than on the other navigation devices. However, today some new receivers can inform its user about jamming incidents by changing the status on dedicated pin. There are also accessible products equipped with a mechanism of transmitting NMEA warning, or function of informing the user about detected abnormal values of S/N ratio, which can suggests jamming. Solution in jamming resistant devices is integration GNSS receiver with Inertial Systems, when mechanism of comparing the coordinates can be implemented. Other way is the usage of very sophisticated receiver with complicated segment-antenna, and Beam-Forming Mechanism, which can create null sections in antenna beam, that signals from some directions will not be received [4]. [2], [3], [6]. By using multiple antenna elements spaced a known distance apart, signal-processing techniques can be employed to discern the direction, from which an interfering signal is arriving, and then adaptively change the apparent receiving strength of the antenna array, creating null gain in source of interference's direction. This idea is implemented into Novatel's (Veripos) GAJT receiver for example.

The main goal using the jammer is to exclude GNSS services in a particular area, and it seems easy to detect by comparison the signal to noise ratio. But the detection of the appearance of disturbances is not enough for locating jammer. In addition, the direction from which an interfering signal is arriving, must become fixed. It is impossible with the standard receiver, as the standard receiving antenna of GNSS receiver's has hemispherical beam pattern, and receive all signals from sources distributed over horizon. Dedicated anti-jamming service should be able, as a minimum to alert users, and it would be desirable, to show direction (or position) in which jammer is situated. Such solution creates the chance of neutralizing the intruder. Nowadays some models of jamming detectors are accessible, however it is not a big market. In the open sources CTL3520, and CTL3510 GPS Jammer Detectors

and Locators of CHRONOS are suggested, however some other are offered too. In this paper one refer to the results of experiments in use ordinary receiver equipped with directional antenna. Detecting the azimuth, or sector in which jammer is located gives the opportunity to determine its location by intersection of two directions determined from two points. An example of such solution can be the Signal Sentry GPS system offered by Harris [10]. The net of two, or more sensors (more sensors gives more accurate results) placed strategically around the port, will instantaneously sense and locate the jamming sources. The data is analysed in real time, the threat type is verified, geolocated, and presented on a web-based visual map. If there are multiple jamming sources present, the system locates each individually.

Authors of this paper found, that the protection of the critical infrastructure from disturbances demanded establish at least two stationary posts with opportunity to determine at least two directions on the source of disturbances, so it gives localization of the area in which jammer is situated. It is possible by using directional antenna with GNSS receiver. We assume that each post will consists of number of receivers equipped with directional antennas [15]. For example, receiving system equipped with three antennas with 180deg sector of beam pattern in the horizontal direction (fig. 1) gives the opportunity to detect the direction in sector of 60 deg. by comparing the signals peer-to-peer.

Let's assume, that in the reception area a signal is available from nine navigation satellites. It seems rational to found that in the region one jammer is located, so signal is transmitted from one direction. Antenna 1, along with a supporting receiving device (signal processor 1) decodes, and processes navigation information from satellites Sv2, Sv3, Sv4, and Sv5. Antenna 2, with a signal processor 2 from: Sv5, Sv6, Sv7, and Sv8, respectively. Antenna 3, with a signal processor 3 from: Sv8, Sv9, Sv1, Sv2, respectively plus a jamming signal. A control and processing device – a navigation processor - continuously analyses, and processes navigation information from all signal processors, and when signals from one of the receiving channels is clearly different from that obtained from the other (as it consists of satellite signals and jammer noise), the channel can be blocked. In this example signals from Sv2 in track 1 (antenna 1 and signal processor 1), and track 3 (antenna 3 and signal processor 3) should differ because of jammer signal presence in track 3. Finally Sv 1 and Sv7 can be skipped in calculations of the position (Sv2 will be received by track 1), but based on the current knowledge about satellites' accessibility the remaining number of satellites is more than 4. The more important is, that this way we know that jammer is located in direction ±30deg from North. For example, if signal will be detected by signal processor 1 and 2 this can be interpreted as jammer is located in the sector between azimuth 300 degrees and 330 degrees.

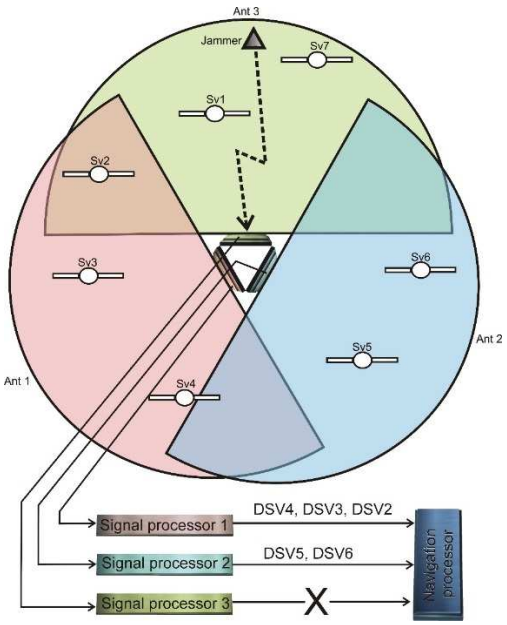

Figure 1. Scheme of device with three antennas, and three parallel receivers.
Source: Felski, 2016

MATERIALS AND METHOD OF EXPERIMENT

In this research we used GPS receivers series R100 of Hemisphere working with helical antennas [21] M1575HCT-22P-SMA of Maxtena Inc. It is a rugged high performance passive antenna designed for the GPS L1 band (fig. 2). An ultra-light (10 grams) screw-on design, featuring an integrated SMA connector. As both, the receiver, and the cabling which we had at our disposal in the laboratory, did not foresee the use of the SMA standard, additionally the transit connectors and the antenna amplifier were used.

Figure 2. Antenna M1575HCT-22P and transition connector.
Source: authors' photo.

Its antenna pattern shape is typical for GNSS antennas (see fig. 3), however its dimension and weight gives opportunity to use its as directional one, if its main axis is oriented horizontally. If so, in horizon it forms almost 180 deg sector, as well in vertical plane – only 90 deg from the horizon plane. We assume, that in such configuration all signals from satellites seated in direction opposite to the orientation of the antenna will not be received, as the radiation generated by jammer. In addition the signals from satellites located in direction of antenna pattern will be received without jammer noise.

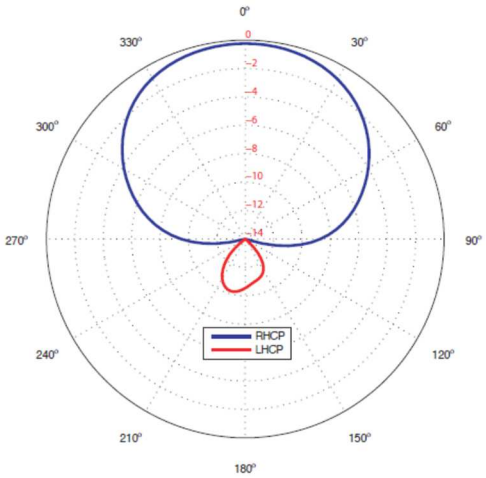

Figure 3. MS575HCT-22 antenna gain plot in vertical intersection.
Source: GPS Helix Antennas

During experiments small, battery powered GPS jammer of Spy Electronics LTD, has been used. It is a device purchased by Internet with (theoretically) 15 meters of radius of activity. [Stopienski, 2020]

Figure 4. Devices applied to experiments: R110 receiver and Spy Electronic jammer.
Source: authors' photo

Receivers were steered with the use of PocketMax4 software, for analysing the local satellite configuration and satellites received by device, we used freely accessible Trimble GNSS Planning software. Example of visualisation of SkyPlot, and received signals with the information about S/N Ratio, is presented on the figure 5. All results and observations were exported to text files with the use of the NMEA 0183 standard, first – the GPGSV message. The message gives the information on the number of visible satellites, their azimuth, the elevation, and the signal strength (see fig. 6).

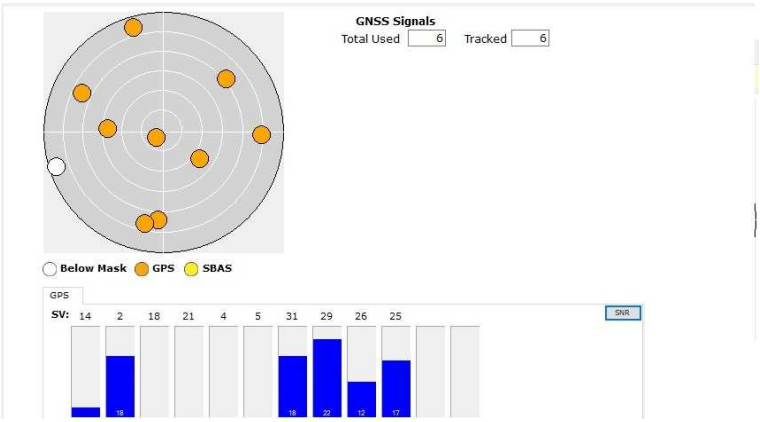

Figure 5. Visualisation of tracked satellites with the standard antenna.
Source: Pocked Max4, authors.

```
$GPGSV,3,1,10,02,42,069,51,06,22,040,,12,47,104,,14,21,268,,*54
$GPGSV,3,2,10,24,04,,,25,81,117,52,26,01,288,33,29,57,24,44,*7D
$GPGSV,3,3,10,31,37,302,47,32,10,246,,,,,,,,*7C
```

Figure 6. Content of GPGSV message adequate to configuration presented on fig. 5.
Source: authors' research.

From the fig. 5 we concluded, that receiver should track 10 satellites with numbers: 02, 06, 12, 14, 24, 25, 26, 29, 31, and 32, however in this example only six (branded in red on the fig. 6) are tracked (02, 14, 25, 26, 29, and 31). Particularly in this example four satellites were shadowed by neighbouring building, and because of that during the next experiments antenna was moved into new place. This example is useful to show how the satellite is presented, which is found within the antenna pattern, however its signal is not taken – after the valuation of the azimuth the value of the signal to the noise ratio should appear. If the signal is not taken, no symbol appears among following commas separating every value (in the fig. 6. for example sat. 06). Figure 6 shows, that over the receiver ten satellites are accessible, all information is divided into three parts and, for example elevation of satellite no 02 is 42 degree, its azimuth is 069 degree and S/N ratio is 51.

On figure 7 the similar information (recorded few minutes later) is presented, but jammer is switched on at the north direction of antenna, at the distance of 10 meters from antenna, and 3 meters over antenna horizon (elevation of about 17 degree over the antenna plane). It must be noticed, that number of tracked satellites dropped from 6 to 3, and S/N ratio dropped down, for example for sat. no 29 from 44 to 35. Important conclusion from similar tests is that low elevation satellite are eliminated by jamming. In this example all satellites below the elevation of 48 degree are eliminated. When active jammer was switched on at the distance closer than 10 meters all signals were blocked in our experiments.

```
$GPGSV,3,1,11,02,22,047,,04,09,336,,05,20,084,,09,01,008*56
$GPGSV,3,2,11,12,17,120,,18,32,182,21,28,192,,25,48,129,35*55
$GPGSV,3,3,11,26,29,296,,29,87,090,35,31,48,262,34,,,,*4F
```

Figure 7. Content of GPGSV message adequate to configuration presented on fig. 5 after the jammer switched on.
Source: authors' research.

The following step of experiments was connection of the helical antenna (situated with main axis almost horizontally, and in azimuth 278 deg.) to the same receiver, and the check of the visibility of satellites. Example of such data is presented on fig. 8. According to the expectations only the part of satellites were tracked, it means only these which were located within the range of the antenna pattern (showed as red sector) oriented in the azimuth of 278 deg.

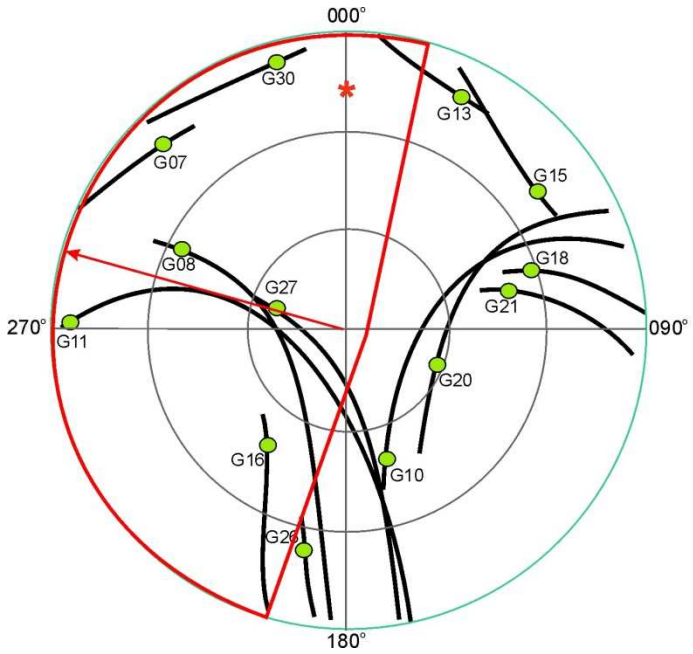

Figure 7. Example of the SkyPlot.
Source: on the basis of Trimble GPS Planner. Red sector present the antenna pattern, red star – jammer.

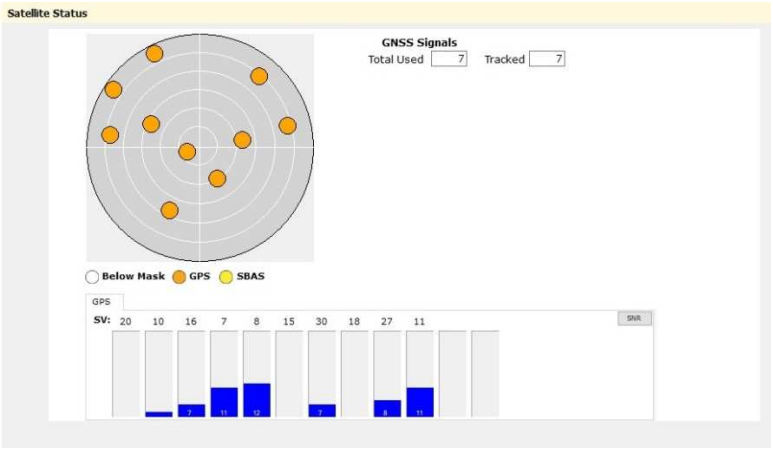

Figure 8. Visualisation of tracked satellites with the helical antenna situated in the horizon plane and in azimuth 278 deg.

In this orientation of the antenna, according to the shape of beam pattern, only six satellite should be tracked. As it is shown on fig. 8 high satellite #10 seems to be

tracked additionally with the use of Pocked Max4, but this is not shown in NMEA 0183 messages (see fig. 9). It is proper to notice that low elevation satellite, for example 7, or 11, possess the very good S/N ratio, while at the use of the traditional antenna, usually such of the satellite show low S/N ratio. Of course this gets out of characteristics of the antenna, when its main axis is not placed vertically.

After the jammer was switched on, only satellite #08 was tracked by the receiver, the other signals were blocked (see fig. 10).

```
$GPGSV,3,1,12,07,09,310,39,08,39,296,41,10,54,157,,11,12,274,41*70
$GPGSV,3,2,12,13,09,020,,15,18,47,,16,41,209,38,18,24,073,,*69
$GPGSV,3,3,12,20,59,091,,21,33,078,,27,74,278,39,30,07,339,36*79
```

Figure 9. Content of GPGSV message adequate to configuration presented on fig. 7, and fig. 8 with helical antenna.
Source: authors' research

```
$GPGSV,3,1,12,07,09,310,,08,39,296,34,10,54,157,,11,12,274,,*51
$GPGSV,3,2,12,13,09,020,,15,18,047,,16,41,209,,18,24,073,,*52
$GPGSV,3,3,12,20,59,091,,21,33,078,,27,74,278,,30,07,339,,*5A
```

Figure 10. Content of GPGSV message adequate to configuration presented on fig. 7, and fig. 8 with helical antenna, and jammer switched on.
Source: authors' research.

In the following example we will talk about the situation when two helical antennas were placed in azimuths 230 and 327 degrees, and was connected to the separate receiver. Jammer, if switched on, was situated in the same place.

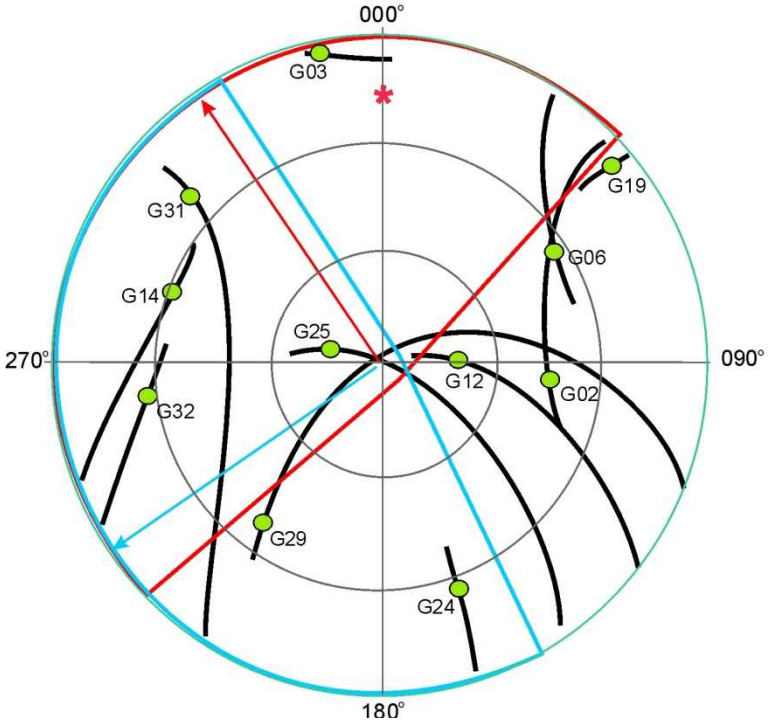

Figure 11. Example of the SkyPlot when two helical antennas are in use.
Source: on the basis of Trimble GPS Planner. Blue sector presents first antenna pattern, and red one – the second.

```
$GPGSV,3,1,11,02,43,094,,03,03,347,,06,32,055,,12,67,091,,*52
$GPGSV,3,2,11,14,28,287,41,19,05,049,,24,22,161,36,25,77,281,36*73
$GPGSV,3,3,11,29,37,217,42,31,21,310,41,32,24,260,36,,,,*44
```

Figure 12. Content of GPGSV message adequate to configuration presented on fig. 10 with helical antenna in azimuth 230deg.
Source: authors' research.

```
$GPGSV,3,1,11,02,43,094,,03,03,347,37,06,32,055,,12,67,091,,*56
$GPGSV,3,2,11,14,28,287,41,19,05,049,20,24,22,161,,25,77,281,36*74
$GPGSV,3,3,11,29,37,217,,31,21,310,41,32,24,260,36,,,,*42
```

Figure 13. Content of GPGSV message adequate to configuration presented on fig. 11 with helical antenna in azimuth 327deg.
Source: authors' research.

Than jammer situated northerly of antennas (red star in the red sector on the fig. 11) was switched on. It caused the disturbance of signals taken by this antenna, and the

blocking of the receiver. However this had no influence on the work of the second receiver, which was connected to second antenna (See figures 14 and 15).

```
$GPGSV,3,1,11,02,43,090,,03,03,349,,06,32,053,,12,65,093,,*5E
$GPGSV,3,2,11,14,28,285,41,19,08,049,,24,20,161,36,25,80,281,33*73
$GPGSV,3,3,11,29,38,220,42,31,24,308,41,32,22,268,36,,,,*4D
```

Figure 14. Content of GPGSV message adequate to configuration presented on fig. 11 with helical antenna in azimuth 230deg., and jammer switched on.
Source: authors' research.

```
$GPGSV,3,1,11,02,43,090,,03,03,349,,06,32,053,,12,65,093,,*5E
$GPGSV,3,2,11,14,28,285,,19,08,049,,24,20,161,,25,80,281,,*5F
$GPGSV,3,3,11,29,38,220,,31,24,308,,32,22,258,,,,*48
```

Figure 14. Content of GPGSV message adequate to configuration presented on fig. 10 8 with helical antenna in azimuth 327deg., and jammer switched on.
Source: authors' research.

When signals were taken through the "blue" antenna, and did not take through the "red" one, jammer is located in the section among 320 and 057 degrees. This confirms the hypothesis that the system designed with sectorial antennas, and separate receivers serving each sections, and also the element comparing signals taken in each tracks assures the detection of jamming events, and settlements of the section, whence this disturbance originate

CONCLUSIONS

Today the threat a jamming of GNSS systems is indisputable. In this article results of experiments with sectorial, and helical antennas were described. These are different from commonly used in the GNSS technique non-directional antennas. Authors hypothesized, that the sectorial pattern of helical antennas allow to limit the jamming, if such antennas will act as the group.

Experiments confirmed the hypothesis that jammer being found outside the section of the activity of the helical antenna did not cause disturbances to the adequate receiver. Our research was passed only with the GPS receiver, however, there cannot be doubts that these rules bear upon all GNSS systems. Of course this is a truth for the certain distance among the jammer, and a receiver, what is mainly determined by the jammer's power.

Similar solution takes place if it is be based on the same number of directional antennas working with separate receivers, or to apply the mechanism of comparing of the relation of the signal to the noise, and the analysis of name of tracked satellites

gives the simple mechanism of the detection of the jamming, and besides this permits to estimate the direction whence comes the disturbance. Examples presented in the paper confirm above.

It became proved, that two antennas situated at the same place, however, directed differently had taken signals from different satellites, and were subject to jamming, or not, depending on the direction wherein the perturbative device was placed. Such solutions would be able to find the use of the installation whose functionality in the critical degree depend on the correct work of GNSS.

REFERENCES

1. Carroll J.V. *Vulnerability Assessment of the U.S. Transportation Infrastructure that Relies on the Global Positioning System*. Journal of Navigation vol.56 issue 2, 2003, pp. 185-193.
2. De Lorenzo D.S., Rife J., Enge P. and Akos D.M. *Navigation Accuracy and Interference Rejection for an Adaptive GPS Antenna Array*. ION GNSS 2006, pages 763-773.
3. De Lorenzo, D.S. *Navigation Accuracy and Interference Rejection for an Adaptive GPS Antenna Array*. PhD Thesis. Department of Aeronautics and Astronautics, Stanford University, US, 2007 (Available at http://waas.stanford.edu/pubs/phd_pubs.html)
4. Digital Beam-Forming Apparatus and Technique for a Multi-beam Global Positioning System (GPS) Receiver Patent US 2008/0291079 A1 2008.
5. *Extreme space weather: impacts on engineered systems and infrastructure*, Royal Academy of Engineering, London, 2013. Available at: https://www.raeng.org.uk/publications/reports/space-weather-full-report (12.09.2014).
6. Fante, RL; Vaccaro, JJ. *Wideband cancellation of interference in a GPS receive array*. IEEE Trans. Aerosp. Electron. Syst 2000, 36, 549–564. [Google Scholar].
7. Felski A., Gortad M. *The significance of an antenna for jamming resistance of a GPS receiver.* Scientific Journal of Polish Naval Academy vol. LVII, no. 4/2016, pp. 5-16.
8. Felski A. *Methods of improving the jamming resistance of GNSS receiver*. Annual of Navigation no. 23/2016 pp. 185-198.
9. GPS Helix Antennas. https://www.maxtena.com/products/helix-antennas/gps-helix-antennas/ (04.08.2020).
10. GPS Interference Detection and Geolocation System. Harris Corporation, 2015. Available at: https://www.ion.org/gnss/upload/files/1525_Harris_PNT_signalsentry_infographic.pdf (04.08.2020).

11. Kraus T., Bauernfeind R. and Eissfeller B., *Survey of in-car jammers – analysis and modeling of the RF signals and IF samples*. In: Proceedings of the 24th International Meeting of the Satellite Division of the Institute of Navigation Portland, 2011.
12. Kuusniemi H., Bhuiyan M. Z. H., Kroger T. *Signal Quality Indicators and Reliability Testing for Spoof-Resistant GNSS Receiver*. European Journal of Navigation vol. 11 no. 2, 2013.
13. McDermott R.N. *Russia's electronic warfare capabilities to 2025*. Republic of Estonia MoD, 2017.
14. Mitch R.H., Dougherty R.C., Psiaki L.M., Powell S.P., O'Hanlon B.W., Bhatti J.A., Humpreys T.E., *"Signal Characteristics of Civil GPS Jammers,"* Proc. Of the 24th Int. Techn. Meeting of the Satellite Division of ION, Portland 2011 Available at: http://gpsworld.com/gnss-systeminnovation-know-your-enemy-12475/ (04.08.2020).
15. Rama Rao B., Kunysz W., Fante R., McDonald K. *GPS/GNSS Antennas*. Artech House Boston, London 2013.
16. Rash. G. D. *GPS jamming in a laboratory environment* Proc. Of the 53rd Annual Meeting of the ION, Albuquerque, 1997.
17. Reports: *North Korea jamming South's air traffic navigation*. Available at: https://news.blogs.cnn.com/2012/05/03/reports-north-korea-jamming-souths-air-traffic-navigation/ (04.08.2020).
18. Scott L.: *Spoofs*, Proofs & Jamming, Inside GNSS, September/October 2012, s. 42-53.
19. Stopienski P. *Opportunity to elimination Jamming by the adequate formation of the antenna beam of the GNSS receiver* (in Polish: Możliwości eliminacji Jammingu poprzez adekwatne kształtowanie wiązki antenowej odbiornika GNSS). Master Thesis. PNA, Gdynia 2020.
20. Truck Driver with GPS Jammer Accidentally Jams Newark Airport. Available at: https://www.scientificamerican.com/article/truck-driver-has-gps-jammer-accident-2013-08/ (04.08.2020).
21. Wang Y-S., Chung S-J. *A miniature Quadrifilar Helix Antenna for Global Positioning Satellite Reception*. IEEE Transactions on Antennas and Propagation. Vol. 57, no. 12, 2009, pp. 3746- 3751

MOŻLIWOŚCI WYKRYCIA ZAGŁUSZANIA ODBIORNIKA GNSS PRZY POMOCY ANTENY ŚRUBOWEJ

STRESZCZENIE

Zagłuszanie sygnałów GNSS traktuje się ostatnio jako istotne zagrożenie dla użytkowników GNSS. Jest to szczególnie niebezpieczne w obliczu powszechnego stosowania systemów typu GPS w życiu codziennym oraz wiary użytkowników w prawdziwość wskazań urządzeń. Mimo prawnego zakazu ich używania jammery są powszechnie dostępne, zwłaszcza w Internecie. Ostatnie lata pokazały jednak, że takie zagrożenie celowo generowały również niektóre organy rządzące, co widać wyraźnie w konfliktach zbrojnych i podczas ćwiczeń wojskowych. Oczywiście stwarza to wielkie zagrożenie dla użytkowników cywilnych, jeśli znajdą się w zasięgu.

Aplikacje i usługi oparte na GNSS są coraz częściej osadzone we współczesnym społeczeństwie, więc społeczność stała się obecnie w decydującym stopniu zależna od ich prawidłowego działania. Dotyczy to przede wszystkim pozycjonowania, ale zależne są też sieci telekomunikacyjne, sieci energetyczne, transakcje finansowe, cały świat logistyki. Główni użytkownicy GNSS, zarówno profesjonalni, jak i nieprofesjonalni użytkownicy smartfonów, nie są przygotowani na taką sytuację i zwykle nie mają technicznych możliwości wykrycia zagłuszania. Dla operatorów instalacji krytycznych, na przykład portów morskich lub lotnisk, wykrywanie przypadków zagłuszania jest niezwykle ważne. Jest to możliwe za pomocą specjalnych urządzeń, które zwykle opierają się na określonych antenach i głębokiej analizie sygnału. W artykule omówiono badania dotyczące wykrywania zagłuszania za pomocą anten śrubowych.

Słowa kluczowe:

Odbiornik GNSS, antena śrubowa.

SCIENTIFIC JOURNAL OF POLISH NAVAL ACADEMY
2020(LXI) 4 (223)

sciendo

DOI: 10.2478/sjpna-2020-0014

TRACKING OF UNMANNED AERIAL VEHICLES USING COMPUTER VISION METHODS: A COMPARATIVE ANALYSIS

Stanisław Hożyń[1] Miłosz Wierszyło[2]*

*[1] *Polish Naval Academy, Faculty of Mechanical and Electrical Engineering, Smidowicza 69, Str., 81-127 Gdynia, Poland; email: s.hozyn@amw.gdynia.pl; ORCID: 0000-0003-1422-0330;*
*[2] *Polish Naval Academy, Faculty of Navigation and Naval Weapons, Smidowicza 69, Str., 81-127 Gdynia, Poland; email: m.wierszylo1995@gmail.com; ORCID: 0000-0001-8277-2183.*

ABSTRACT

Tracking of small objects in any given airspace is an integral part of modern security systems. In these systems, there are embedded methods that employ the techniques based on either radio waves, or acoustic signals, or light radiation. The computer vision operation, springing from the light radiation-based technique, has prompted interest in its research. This operation has the advantage of being less expensive than radars and acoustic systems. In addition, it can solve complex security problems by detecting and tracking humans, vehicles, and flying objects. Therefore, this article evaluates the usefulness of the varying computer vision algorithms for tracking of small flying objects.

Keywords:
unmanned aerial vehicle (UAVs), computer vision, object tracking.

Research article

INTRODUCTION

Unmanned aerial vehicles' (UAVs) incursion of the critical infrastructure constitutes one of the most significant security-related challenges. Enhancing the detection, and tracking of UAVs increases the defence against such an incursion, and therefore provides the necessary protection for strategic facilities. There are three choices that aid the enhancement outcome, and they are either radio waves, acoustic signals, or visible light.

Radio waves, employed in radar systems, are used to detect objects in the airspace in both civil, and military aviation. Radar works on the principle of emitting electromagnetic waves, which, after reaching the object, are reflected, and returned to the receiver providing information about the object location. By utilising the phenomenon that a radio beam reflects from materials, such as metal and carbon fibre, the majority of flying objects can be detected [1]. In this process, the stable frequency generators and precise measurement of the time between sending a receiving signal are demanded [2]. Among the radio wave techniques, one of the state-of-the-art solutions uses the Phase-Interferometric Doppler Radar that facilitates creating 3D maps of the supervised area. The maps depict the detected objects, their range, velocity, and azimuth angles. The signal processing stage is divided into two parts: the Range-Doppler Processing, and Range Azimuth Processing. By using two receiving channels, the radar configured with phase-interferometry is able to estimate the angle of arrival (AOA) [3].

Acoustic systems analyse sound emitted by the object in order to detect the direction of signal emission. They do not require seeing the object during operation, which allows to use them in urban facilities, or behind hills [4]. In this respect, acoustic systems outperform other methods based on radio waves and visible light. What is more, the weather conditions, and the part of the day do not impede the detection process [5]. Acoustic systems usually comprise arrays of sensitive microphones. A large number of microphones, and advanced digital signal processing enable determination of azimuth, and elevation of the target in real-time. Another advantage involves modularity and scalability, which allow the use of this type of detection in combination with other systems [6].

The significant progress of computer vision technique has been demonstrated in many research areas, such as intelligent surveillance systems, autonomous vehicles, or industrial automation [7–10]. Cheaper cameras and faster computers, as well as more sophisticated algorithms, facilitate engaging computer vision in a wide range of real-time applications [11]. In case of protection against UAVs' attacks, these systems are responsible for the detection, and tracking of suspicious objects. They cost less than radars and acoustic systems. What is more, their highly complex solution systems have the ability to detect, recognise, and track various targets, such as humans, vehicles, or flying objects in any surrounding area [12].

The detection step often utilises advanced object detection algorithms, implemented in computer vision libraries. In [13], the comparative analysis of these

algorithms, applied in the OpenCV libraries, was performed. The algorithms were divided into two main groups – supervised classifiers, and background subtractors. The first group included algorithms, such as the KNN, Codebook, and Codebook 2, while the second group comprised the MOG, MOG2, and GMG. According to the research, the MOG algorithm was the best choice for UAVs detection [13].

Detection of suspicious objects constitutes a crucial step in surveillance systems. However, when the object is detected, its location should be monitored. To perform this task, tracking methods, enabling real-time execution with high accuracy, are implemented. Plenty of algorithms dedicated to object tracking have been presented in the literature. Among the most popular ones can be enumerated: the Dense Optical Flow, Sparse Optical Flow, Kalman Filtering, Mean Shift, Cam Shift, Single Object Trackers, and Multiple Object Trackers. Since they differ in accuracy and complexity, the preliminary research was devoted to distinguishing the group of the methods which are promising in view of UAVs tracking. For that reason, each method was tested on short samples of movies, and evaluated using human eye examination. Consequently, the following methods were taken into further consideration: the CSRT Tracker [14], MIL Tracker [15], MOSSE Tracker [16], and KCF Tracker [17].

This article presents a comparative analysis of selected algorithms applied in object tracking in order to assess their usefulness for tracking of UAVs. First, the algorithms with their mathematical processes are described. Then the results of the experiments are presented, and, finally, the conclusions are formulated.

METHODS

The aim of the work was to assess the usability of the selected object tracking methods for the USVs defence system. A short description of the chosen algorithms is provided below.

CSRT Tracker

The CSRT algorithm, proposed by Alan Lukezic, is based on the DCF procedure. It improves the accuracy of the DCF tracker by adding spatial reliability maps. The use of the spatial reliability maps allows tracking more complex targets because the channels are combined to establish the final response map [5]. The execution of the algorithm can be divided into three stages:

- Scale location.
- Scale estimation.
- Updating operation.

Scale location and estimation select features from the search region, which is centred on the target estimated position in the previous time step, and correlated with the filter. In the updating step, the training region is centred on the previously

estimated target location. Then, the foreground and background histograms are extracted, and updated by the exponential mean with the learning rate. After extracting the foreground $\tilde{\mathbf{c}}^f$ and background $\tilde{\mathbf{c}}^b$ histograms, the algorithm updates these histograms, utilising the formula presented below [6]:

$$\mathbf{c}_t^f = (1-\eta)\mathbf{c}_{t-1}^f - 1 + \eta\tilde{\mathbf{c}}^f, \tag{1}$$
$$\mathbf{c}_t^b = (1-\eta)\mathbf{c}_{t-1}^b - 1 + \eta\tilde{\mathbf{c}}^b, \tag{2}$$

where:
η – learning rate,
$\mathbf{c}_{t-1}^f$ – foreground histogram of the previous frame,
$\mathbf{c}_{t-1}^b$ – background histogram of the previous frame.

The next step is to calculate the channel reliability **w:**

$$\mathbf{w} = \mathbf{w}^{(\mathrm{lrn})} \times \mathbf{w}^{(\mathrm{det})}, \tag{3}$$

where:
$\mathbf{w}^{(\mathrm{lrn})}$ – reliability of the learning channel,
$\mathbf{w}^{(\mathrm{det})}$ – reliability of the detection channel.

The last step updates the filter, and channel reliability using the following equations:

$$\mathbf{h}_t = (1-\eta)\mathbf{h}_{t-1} + \eta\mathbf{h}, \tag{4}$$
$$\mathbf{w}_t = (1-\eta)\mathbf{w}_{t-1} + \eta\mathbf{w}, \tag{5}$$

where:
$\mathbf{h}_{t-1}$ – filter calculated for the previous frame,
$\mathbf{w}_{t-1}$ – reliability of the channel of the previous frame

MIL Tracker

The MIL Tracker algorithm represents supervised learning in which training instances are arranged in sets called bags. The training set consists of many bags containing instances. The bag is positively labelled if it has at least one positive case. Otherwise, the bag is marked negatively. The task of the method is to learn the concept from the training kit for the correct labelling of bags [7].

The MIL algorithm uses a gradient-increasing structure to train the classifier to maximise the occurrence of positive cases. This operation is executed according to the formula presented below [8]:

$$\log L = \sum_i (\log p(y_i|X_i)), \tag{6}$$

where:
L – plausibility function,
$p(y_i|X_i)$ – likelihood of a positive bag.

The probability is determined for bags, not for instances, because the labels of instances are not known during training. The last step of the algorithm is to determine the probability of a positive bag. In this case, the Noisy-OR model, described by the formula below, is adopted [8]:

$$p(y_i|X_i) = 1 - \prod_j \left(1 - p\left(y_i|x_{ij}\right)\right). \tag{7}$$

MOSSE Tracker

The MOSSE tracker utilises correlation filters. By using adaptive correlation for object tracking, it generates stable correlation filters utilising only one frame. This leads to high performance by computing time-domain correlations. The tracking module is resistant to variable lighting conditions, as well as the object's movement and its deformation. The module calculates the minimum square error output to find the most precise location of the target [5].

The shape of the object is assumed to have a two-dimensional Gaussian distribution. Regarding the baseline image, the top of the distribution is located in the centre of the input picture. To find the filter template H, the algorithm uses the square of the sum of the output convolution, and determines the output error of the convolution using the following operation [9]:

$$H = \min_H \sum_i |F_i \odot H^* - G_i|^2, \tag{8}$$

where:
F_i – pre-processed template,
H^* - complex filter conjugate,
G_i – image of the object,
$\odot$ - elementary multiplication symbol.

In order to increase the learning speed, the algorithm raises the weight of the previous frame, and allows it to spread exponentially. The filter adapts to changes of the object's appearance by determining the coefficients using the following formulas [9]:

$$A_i = \eta G_i \times F_i^* + (1-\eta)A_{i-1}\,, \tag{9}$$
$$B_i = \eta F_i \times F_i^* + (1-\eta)B_{i-1}, \tag{10}$$

where:
F_i^* - the complex conjugate of the processed template.

The coordinates of the highest point in the result are recognised as the target at the frame's current position; thus, the new target is used to update the filter template. The above process is repeated for continuity in tracking [9].

KCF Tracker

The concept of this tracker assumes that many positive samples have large overlapping regions. The module uses these regions to speed up tracking, and to obtain the highest accuracy. The number of calculations is reduced by the properties of the circulating matrix and the kernel function. Additionally, the prediction of unidentified data is performed by linear ridge regression, based on the machine learning solution. The set of sample images is denoted as a_i, while the variable z_i takes the value +1 if the object is present in the image, and -1 if the object is imperceptible. Subsequently, the normalised ridge regression, based on square loss and square regulation, is used. It is a convex function with a unique solution, which can be represented as [11]:

$$w = (\mathbf{A}^T\boldsymbol{A} + \lambda I)^{-1}\boldsymbol{A}^T\mathbf{z}, \tag{11}$$

where:
$\boldsymbol{A}$ – matrix comprising of all the vectors used for training,
$\mathbf{z}$ – vector consisting of appropriate values z_i.

The circulating matrix $\mathbf{C}(\mathbf{a})$ obtains its values using the discrete Fourier transform [11]:

$$\mathbf{C}(\mathbf{a}) = Udiag(\hat{a})U^*, \tag{12}$$

where:
$diag(\hat{a})$ – the diagonal matrix containing the DFT coefficients of vector **a,**
U – the value of the discrete Fourier transform.

RESULTS AND DISCUSSION

This section presents a comparative analysis of the described algorithms. The algorithms were tested to determine their tracking accuracy and efficacy. In order to carry out research, the algorithms were implemented using the C++ language, as well as OpenCV and Qt libraries. The trackers were tested on video sequences, in which the movement of UAVs differed in respect of speed, dynamics, and distance from the camera. Additionally, various weather and lighting conditions were taken into consideration. One frame of the first sequence is shown in Fig. 1.

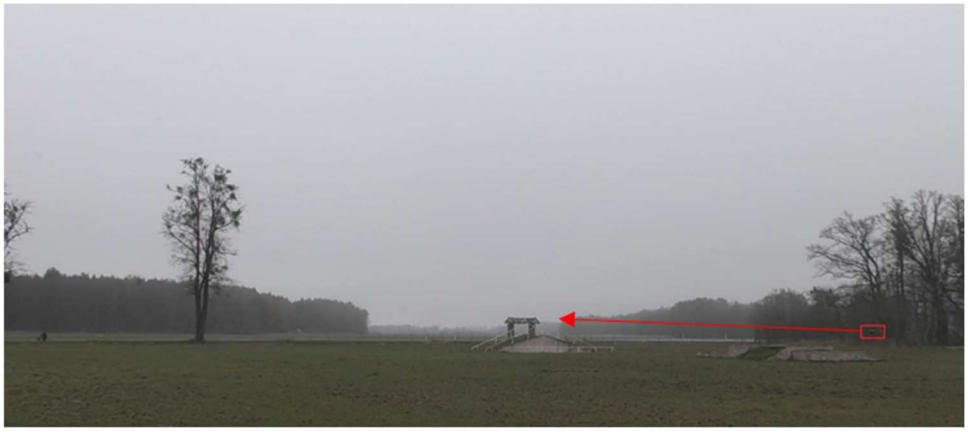

Fig 1. An exemplary frame of the first sequence. [own work]

Research results

Efficacy was the first analysed parameter. It was calculated as the ratio of the number of frames containing the correctly tracked object to the total number of frames in the sequence. Since in our work, we focused on tracking methods, the position of the object was manually marked in the first frame of the sequences.

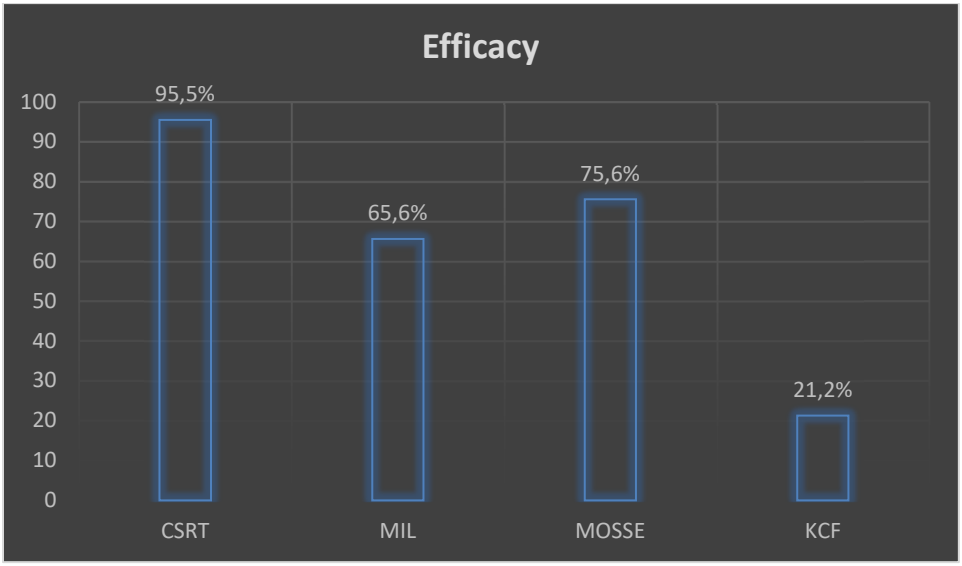

Fig 2. Efficacy of the tested algorithms. [own work]

The results of the conducted experiments are depicted in Fig. 2. They show that the CSRT algorithm tracked the object with very high accuracy, reaching ninety-six per cent. The MOSSE and MIL algorithms obtained about seventy per cent accuracy, which is a poor result for developing a reliable tracking application. The KCF method achieved only twenty-one per cent accuracy.

The next analysed parameter was the average processing time of a single frame in the analysed sequences.

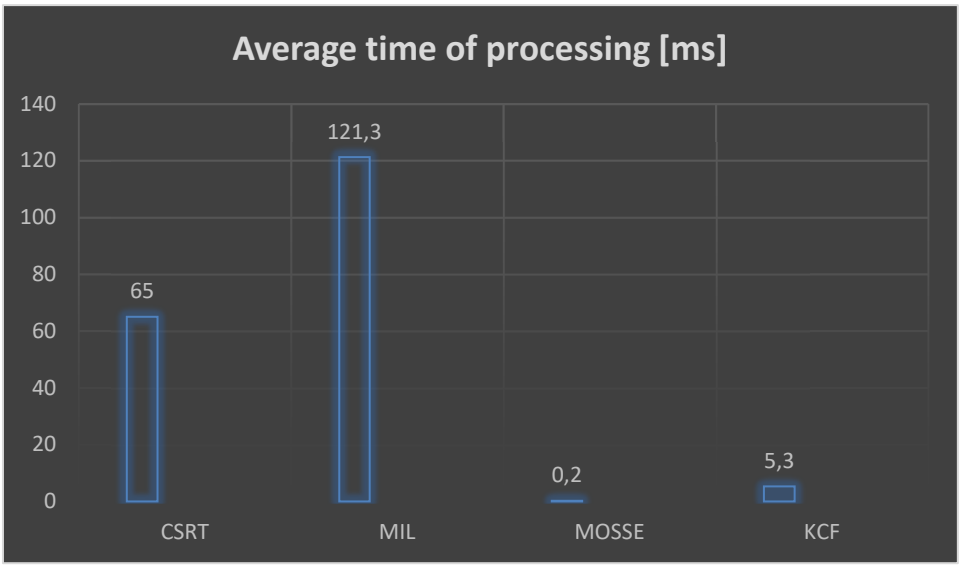

Fig 3. Average processing time of the tested algorithms. [own work]

In this case, the MOSSE module outperformed the other algorithms, achieving a time of 0.2 ms. The KCF algorithm also performed very quickly, while the CSRT and MIL methods were much slower (see Fig. 3). Even though the execution time of the MIL method amounted 121 ms, we assumed it as sufficient for real-time tracking applications.

The third analysed parameter was the shortest single frame processing time. The obtained results were in line with the average time, and proved that the MOSSE

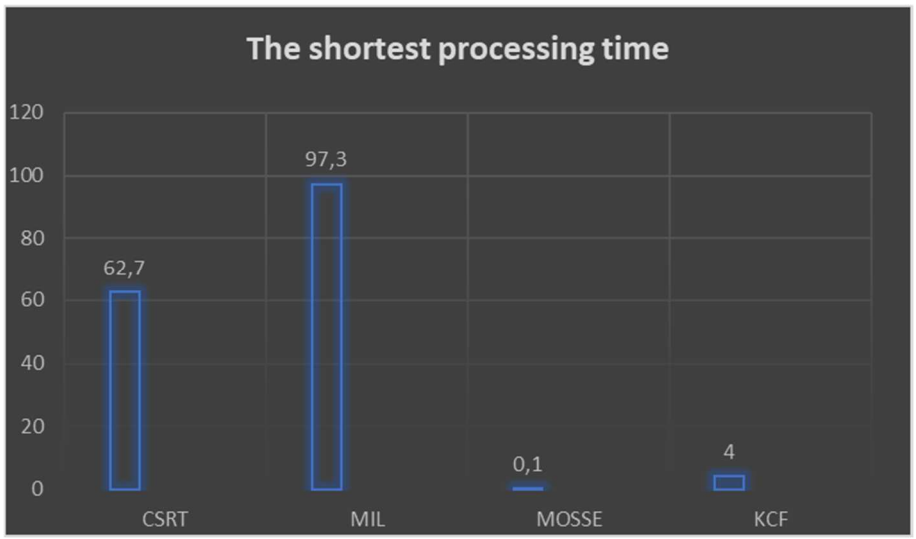

Fig 4. The shortest processing time of the tested algorithms. [own work]

and KCF methods are the fastest ones, while the MIL and CSRT methods execute much slower (Fig. 4).

The last investigated parameter was the longest processing time of a single frame in the tested sequences.

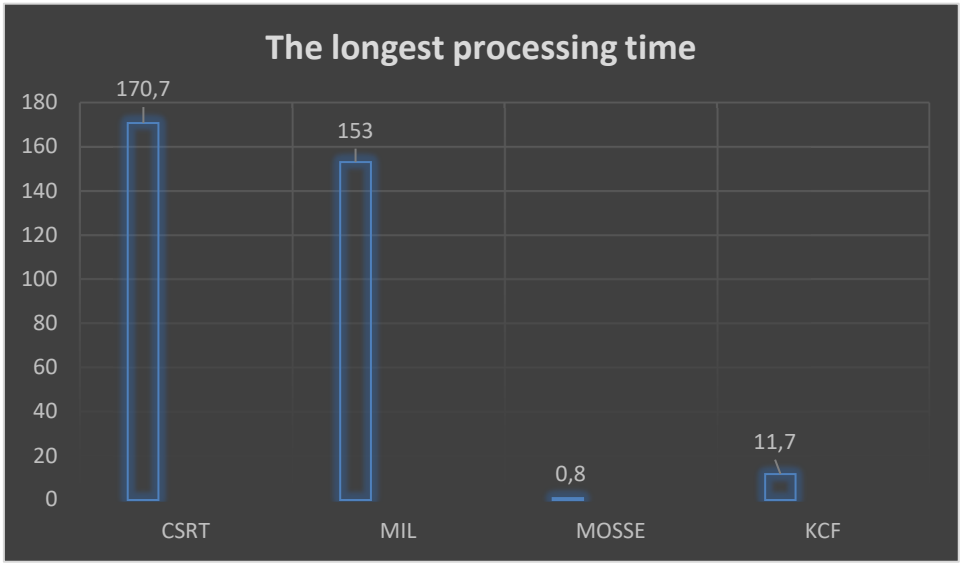

Fig 5. The longest processing time of the tested algorithms. [own work]

In this case, the CSRT and MIL algorithms executed significantly slower than the MOSSE and KCF methods. The longest processing time, amounted to 171 ms, was achieved by the CSRT algorithm, while the shortest time, equals to 0.8 ms, was obtained by the MOSSE method (see Fig. 5).

In our analysis, efficacy posed the most crucial factor because it determined the ability of the method to perform tracking of UAVs. Taking into consideration the characteristics of UAVs' movement, as well as weather, and lighting conditions, we acknowledged the CSRT method as the most appropriate for UAVs tracking applications. Even though its execution time varied from 63 to 171 ms, it may be applied for real-time application since longer time did not impede the UAVs tracking performance.

The MOOSE method executed very quickly. Consequently, improvement of its accuracy would make it suitable for fast real-time applications. The improvement could be achieved by adding additional image pre-processing steps, allowing a better distinction of UAVs from the background. We assume, that efficacy that is higher than ninety per cent will facilitate tracking with a high level of confidence. Additionally, in the case when higher efficacy was difficult to achieve, the cooperation of object detection and tracking algorithms would be considered. It would be convenient due to the short execution time of the MOOSE method. What is more, the efficacy of this algorithm could be improved with position estimators such as the Kalman, or Particle filters.

The performance of the MIL and KCF methods was lower than the CSRT and MOSSE methods. The MIL algorithm was the slowest one, whereas the KCF method achieved the lowest efficacy. Consequently, they are less suitable for real-time UAV applications.

CONCLUSIONS

Analysis of the above algorithms has shown that the CSRT algorithm is the best choice for UAVs tracking. Although the algorithm was not the fastest one, it outperformed other algorithms in the quality of efficacy. The MOSSE method, which was very fast, achieved seventy-six per cent efficacy. This efficacy is too low for tracking applications, but it can be improved using image pre-processing steps, cooperation with detection algorithm, or the Kalman and Particle filters. Therefore, additional experiments are needed to evaluate its effectiveness in real-time tracking applications. The MIL and KCF methods appeared to be unsuitable for UAVs tracking.

By combining the MOG algorithm for detection, and the CSRT algorithm for tracking, the backbone of an autonomous security system can be developed. In combination with modern vision systems, the effective, and efficient monitoring solution for essential infrastructure can be achieved.

The presented research has been carried out under daylight conditions. Since night conditions determine utilising an infrared camera, future work will focus on selecting the most suitable methods for UAVs detection, and tracking on thermal images.

REFERENCES

[1] Wąż, M.; Naus, K. *Wizualizacja wielowymiarowego obrazu radarowego*. Zesz. Nauk. Akad. Mar. Wojennej 2013, *195*, 99–116, doi:10.5604/0860889X.1097972.

[2] Blok, M.; Kaczmarek, S.; Młynarczuk, M. *Radar Data Fusion in the Stradar System*. Sci. J. Polish Nav. Acad. ***2019***, *218*, 43–56, doi:10.2478/sjpna-2019-0017.

[3] Yoon, J. H.; Xu, H.; Garcia Carrillo, L. R. *Advanced Doppler radar physiological sensing technique for drone detection*. In; Ranney, K. I., Doerry, A., Eds.; **2017**; pp. 10–21.

[4] Piskur, P.; Szymak, P. *Algorithms for passive detection of moving vessels in marine environment*. J. Mar. Eng. Technol. 2018, *16*, 377–385, doi:10.1080/20464177.2017.1398483.

[5] Sutin, A.; Salloum, H.; Sedunov, A.; Sedunov, N. *Acoustic detection, tracking and classification of Low Flying Aircraft*. In *2013 IEEE International Conference on Technologies for Homeland Security (HST)*; IEEE, 2013; pp. 141–146.

[6] Dumitrescu, C.; Minea, M.; Costea, I. M.; Cosmin Chiva, I.; Semenescu, A. *Development of an Acoustic System for UAV Detection*. Sensors 2020, *20*, 4870, doi:10.3390/s20174870.

[7] Hożyń, S.; Zalewski, J. *Shoreline Detection and Land Segmentation for Autonomous Surface Vehicle Navigation with the Use of an Optical System*. Sensors 2020, *20*, 2799, doi:10.3390/s20102799.

[8] Praczyk, T.; Hożyń, S.; Bodnar, T.; Pietrukaniec, L.; Błaszczyk, M.; Zabłotny, M. *Concept and first results of optical navigational system*. Trans. Marit. Sci. 2019, *8*, 46–53, doi:10.7225/toms.v08.n01.005.

[9] Hożyń, S.; Żak, B. *Local image features matching for real-time seabed tracking applications*. J. Mar. Eng. Technol. 2017, doi:10.1080/20464177.2017.1386266.

[10] Maan, S.; Tyagi, A.; Kumar, S.; Kumar, A. *Security and Surveillance using Computer Vision*. Int. J. Comput. Appl. 2020, *176*, 30–35, doi:10.5120/ijca2020920280.

[11] Hożyń, S.; Żak, B. *Moving Object Detection, Localization and Tracking Using Stereo Vison System.* Solid State Phenom. 2015, *236*, 134–141, doi:10.4028/www.scientific.net/SSP.236.134.

[12] Gautam, K. S.; Parameswaran, L.; Thangavel, S. K. *Computer Vision Based Asset Surveillance for Smart Buildings.* J. Comput. Theor. Nanosci. **2020**, *17*, 456–463, doi:10.1166/jctn.2020.8691.

[13] Hożyń, S.; Przybysz, M. *Detection of Unmanned Aerial Vehicles Using Computer Vision Methods: A Comparative Analysis*. Sci. J. Polish Nav. Acad. 2020, *220–221*, 5–13, doi:10.2478/sjpna-2020-0001.

[14] Lukežič, A.; Vojíř, T.; Čehovin Zajc, L.; Matas, J.; Kristan, M. *Discriminative Correlation Filter Tracker with Channel and Spatial Reliability*. Int. J. Comput. Vis. **2018**, *126*, 671–688, doi:10.1007/s11263-017-1061-3.

[15] Babenko, B.; Ming-Hsuan Yang; Belongie, S. *Robust Object Tracking with Online Multiple Instance Learning*. IEEE Trans. Pattern Anal. Mach. Intell. 2011, *33*, 1619–1632, doi:10.1109/TPAMI.2010.226.

[16] Bolme, D.; Beveridge, J. R.; Draper, B. A.; Lui, Y. M. *Visual object tracking using adaptive correlation filters.* In 2010 IEEE Computer Society Conference on Computer Vision and Pattern Recognition; IEEE, **2010**; pp. 2544–2550.

[17] Henriques, J. F.; Caseiro, R.; Martins, P.; Batista, J. *High-speed tracking with kernelised correlation filters*. IEEE Trans. Pattern Anal. Mach. Intell. 2015, *37*, 583–596, doi:10.1109/TPAMI.2014.2345390.

ANALIZA METOD ŚLEDZENIA BEZZAŁOGOWYCH STATKÓW POWIETRZNYCH WYKORZYSTUJĄCYCH TECHNIKI WIDZENIA KOMPUTEROWEGO

STRESZCZENIE

W artykule przedstawiono analizę metod śledzenia bezzałogowych statków powietrznych, wykorzystujących techniki widzenia komputerowego.

Słowa kluczowe: Bezzałogowy statek powietrzny, widzenie komputerowe, śledzenie obiektów.

SCIENTIFIC JOURNAL OF POLISH NAVAL ACADEMY
2020 (LXI) 4 (223)

sciendo

DOI: 10.2478/sjpna-2020-0015

MOBILE WHEELED ROBOT TO SUPPORT THE TASK OF THE ALARM SUB-UNIT

Daniel Powarzyński*

* *Polish Naval Academy, Faculty of Mechanical and Electrical Engineering, Smidowicza 69, Str., 81-127 Gdynia, Poland; email: danielpow@interia.pl;*

ABSTRACT

The article is a presentation, and detailed description of a mobile, vehicular robot whose task is to support the alarm sub-unit. The project was created in response to the increasing need for monitoring, and recognition of the areas. The robot's interface was created with the use of integrated development environments for Python. The software implementation was possible due to a minicomputer Raspberry Pi 4 B. The robot's frame is made out of components which are based on the main chassis. The robot is equipped with compatible sensors and cameras. Those, combined with the interface, are able to give a real-time preview of the area in which the robot is in.

This particular vehicular robot is designed to eliminate the risks caused by tasks of alarm sub-unit, by giving the real-time preview, and analysis of the currently watched area. In addition, it can be used to inspect soldiers in the containment zones, and to help with the identification of unknown objects.

Keywords:

mobile robot, raspberry pi, phyton, controlling a mobile robot

Research article

INTRODUCTION

Mobile robots are more common in civilian [3], and military case [14] scenarios. Because of their advantages, such as mobility, autonomy, manoeuvrability, and upgrading abilities they are a great option, if not an essential alternative, to human input. They can easily cover tasks traditionally made for people.

Advanced robots [17] can do more complicated tasks, and lower the possibility of unwanted loss at the same time. Thanks to high-quality materials [4], manipulators, sensors, and vision cameras those robots can be both fully functional, and precise. Their multitasking abilities are highly valued, especially when it comes to engineering, and minesweeping tasks. Artificial intelligence-based software [12], combined with cameras and sensors, allows the proper identification of objects and enemy firepower. It is also worth noting, that frequently mounted manipulators are essential in the context of explosive ordnance disposal missions. They are useful when it comes to neutralizing and moving explosive charges.

When it comes to mobile robots, PIAP PATROL [21] (Fig. 1) seems to be a perfect example. It is a medium-sized caterpillar track-type robot whose purpose is to detect any chemical, biological, radiological, and nuclear hazards. It can also identify and neutralize counter improvised explosive devices (C-IED). Due to the applied caterpillar drive, the robot can operate both inside, and outside, and achieves a top speed of 8km/h. The robot has 2 meters long, 6-graded manipulator, which can pick up, and lift objects to 22 kg. Also, the robot may have radiation sensors. They can spot, and identify chemical warfare agents, and fumes coming out of explosive charges.

Another example of a robot, that is out on the civil market, is SUMMIT-XL HL [22] (Fig. 2). It is a highly versatile mobile platform intended for indoor and outdoor use. Moving heavy loads is its designed use. The robot can be programmed and move autonomously, or manually with the aid of a remote control. Real-time preview is achievable through an installed PTZ camera. The robot is equipped with angle sensors too. They allow avoiding collisions by calculating the distance between the robot itself and an object.

The article presents programmed software, and engineering of vehicular mobile robots intended to support tasks of alarm sub-unit, as well as implementations of the system with real-time preview.

Fig. 1 PIAP PATROL [21]

Fig. 2 SUMMIT XL-HL [22]

ALARM SUB-UNIT

Alarm sub-unit is a military authority dedicated to:

- supervising, patrolling of the designated route (Fig. 3), and protecting military units
- securing crime scenes, and preventing the attempts to cover the traces of a crime, or to erase the evidence of crimes
- supporting and securing enterprises from the "Catalogue of extraordinary incidents, accidents, and breaches of military discipline reported to Operational Duty Service of the Secretary of Defence"
- securing intervention areas in cases of violation of military law, disturbance of safety, or supervising public order inside the military unit

All the above mentioned alarm sub-unit tasks can be supported by a mobile robot. Recording of any events allows soldiers to adapt better. At the same time, all records can be used as evidence, and provide materials to analyse any emergencies.

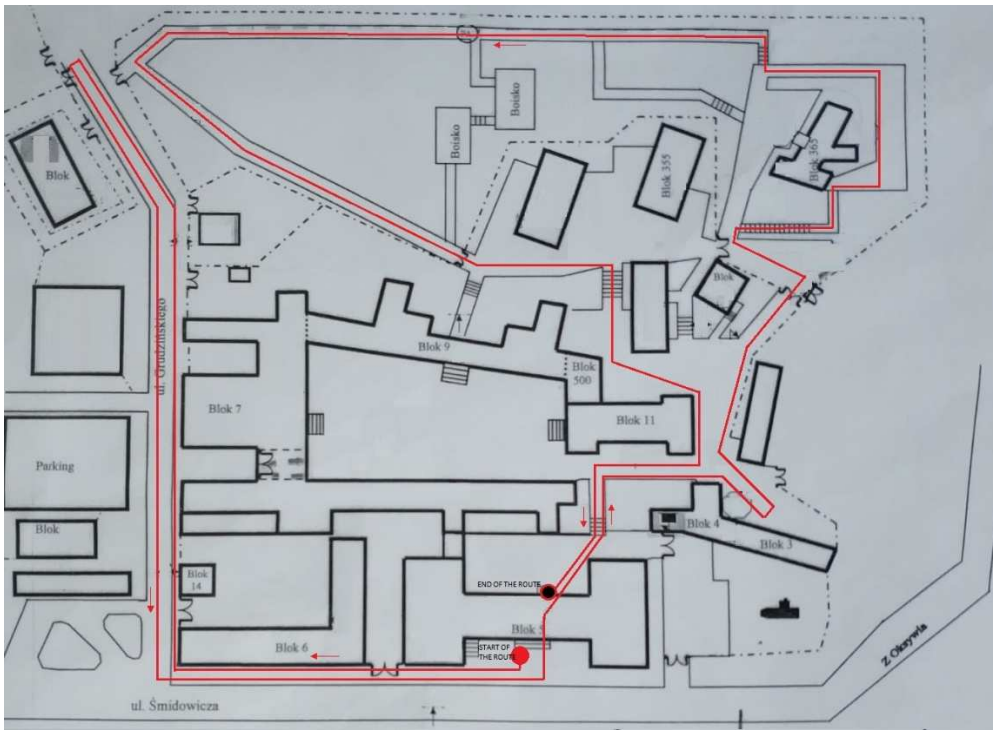

Fig. 3 External patrol route of a mobile robot

ROBOT STRUCTURE

The robot is based on a component frame. Because of that, every used hardware has to be lightweight, compatible with each other, and durable at the same time. Chassis is the main steel plate, and the most resilient item in the structure.

Front suspension with control system (Fig. 4 pt.1) has pieces that altogether allow connecting wheels, and shock-absorption system with the rest of the vehicle. The shock absorption in the suspension system is responsible for the stability and manoeuvrability, and is necessary when it comes to overcoming any obstacles. The suspension is built by connecting two co-working swing arms, shock absorbers springs, and stub axles. The structure of the rear suspension is similar to the one on the front, but because it is a rear-wheel drive, the whole suspension connects to the drive train (Fig. 4 pt.2). To make it move, putting wheel hubs, bearings, and semi-axis was required.

Drive train system is working through three cogwheels based on bearings. All of that sits inside a hermetic case made out of Polyamide. On the external ends of the shafts are flywheels connected to a driveshaft. 72-teeth disc wheel, mounted on

the main gear shaft, transfers the drive from the engine.

The main sub-components of the drive train are the electric brush motor RS-540SH (Fig. 4 pt. 3), and the drive wheel. They transmit the spin to a disc wheel. Combining optimised torque with well-balanced energy consumption allows obtaining both a good speed, and a long-lasting operative time. The engine is absorbing between 4.8-7.2 V with 23400rpm.

Mechanical speed controller (Fig. 4 pt.4) is responsible for accelerate, braking, and reversing. It keeps getting power from the battery, and sends it to the engine through the wires. The main parts of the controller are the spinning disk, reaction arm, and electric circuit. The mechanical speed controller connects to a resistor (Fig. 4 pt.5), which lowers the power voltage delivered from the battery to the engine. The resistor itself is surrounded by a radiator, which sends down the heat coming from electricity flow.

Servo-controllers are the ones responsible for fulfilling tasks, such as steering and turning wheels. The throttle servo-controller (Fig. 4 pt.7) converts electricity into a mechanical movement that is passing to the mechanical speed controller. The steering servo-controller (Fig. 4 pt.6) is responsible for front wheel movement. The power needed to run every component comes from the “Redox” nickelic-metal-hydrogen battery (Fig. 4 pt.8).

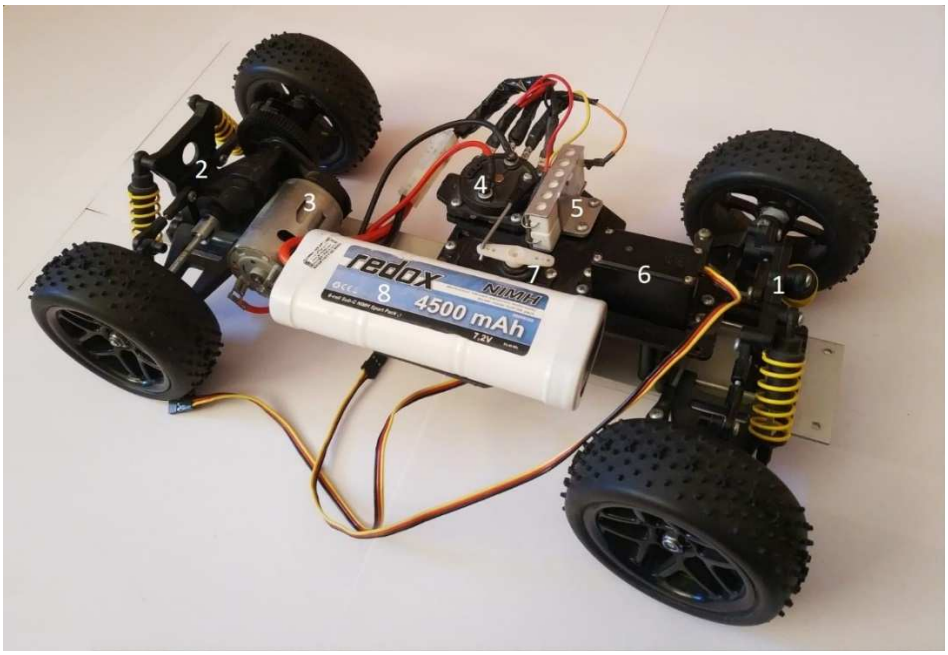

Fig. 4 Structural skeleton of a mobile robot

1 – front suspension system, **2** – rear suspension system with the drive train, **3** – electric engine RS-540SH, **4** – mechanical speed controller, **5** – resistor with heat sink **6** – steering servo controller, **7** – throttle servo controller, **8** – battery

ASSIST CONTROL SYSTEM – ULTRASONIC SENSORS SH-SR004

Two ultrasonic distance sensors HC-SR004 [20] are responsible for avoiding collision autonomously. Distance system measures the time between sending, and return of the ultrasonic wave. The microcontroller receives information about the distance. Aspects like sunlight, or dark colour of objects do not impact the way the sonar works. Sensors have 4 outlets VCC, GND, ECHO, and TRIG. To start measurement initiation, pin TRIG needs to receive 5V electrical pulse for 10 μs. Afterwards, the sensor sends eight pulses with 40 kHz frequency to measure the distance. A wave hits an encountered obstacle, and returns to the sensor. That signal is called echo. After the measurement, the pin ECHO receives the signal, and after that, the real measurement begins. How long it will take depends on the distance between the robot and obstacle. Range hovers between 150 μs to 25 ms. Receiving data takes up to 38 ms. The distance *d* is calculated according to the equation (1).

$$d = \frac{T * v}{2} \tag{1}$$

where:

d – distance [m]

T – the time interval between sending trigger signal, and receiving echo signal [s];

v – the velocity of sound [m/s].

The individual sensor can do the correct measure in between the 30-degree angle (Fig. 5). Most important is to set the sensors so that they do not overlap each other. If set incorrectly, they will distort the received signal. In consequence, the robot will do the wrong measurements, and it will not avoid an obstacle. Sensors should be placed opposite with +/- 45^{o} (Fig. 6) against the front suspension.

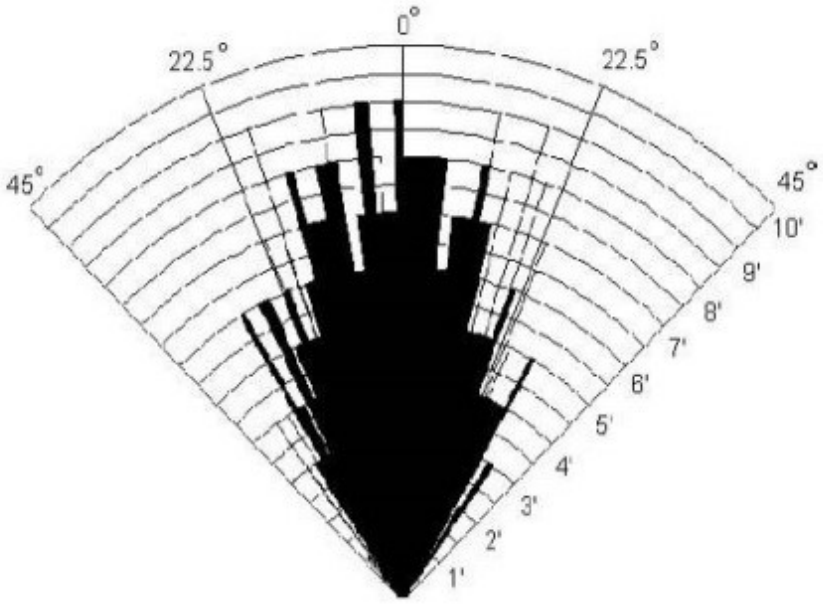

Fig. 5 Sensor measurement angle [20]

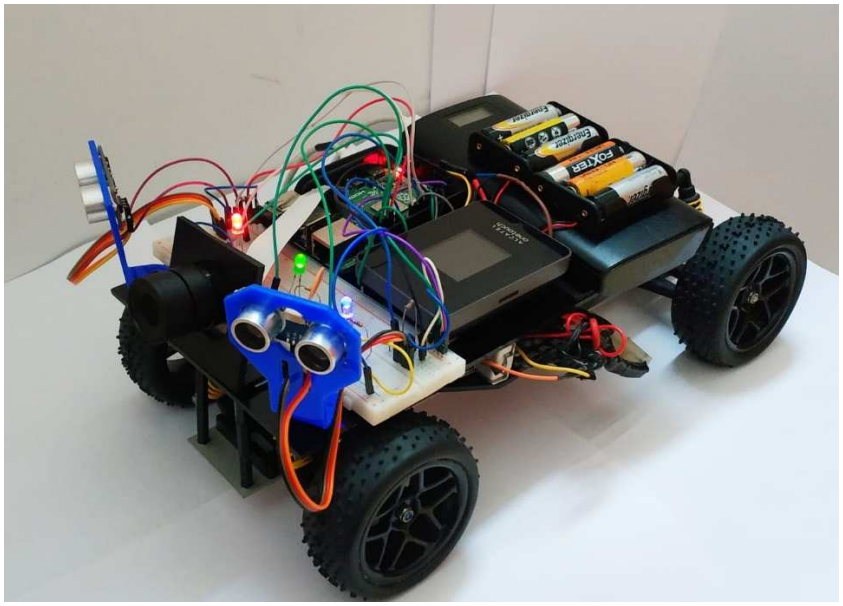

Fig. 6 Final construction of a mobile robot

IMPLEMENTATION

Hardware platform allows the user to control the robot by programming its movement. Responsible for that is a minicomputer Raspberry PI 4 B running on Broadcom BCM2711 network. It has 64 bit processor quad-core 64 ARM-8 CortexA72 with 1.5GHz frequency. The chosen programming language is Python, which allows the structure, function and object programming.

```
#Libraries used
import time
import sys
import RPi.GPIO as GPIO
import os
from echo import distance_thread
import threading
from distance import Czujnik
from pynput.keyboard import Listener, Key, Controller
#Pins designation
DISTANCE_LED_PIN = 40
READY_PIN = 38
CAM_ON_PIN = 36
SERVO_1_PIN = 10
SERVO_2_PIN = 11
#Pins initialization
GPIO.setmode(GPIO.BOARD)
GPIO.setup(DISTANCE_LED_PIN, GPIO.OUT)
GPIO.setup(READY_PIN, GPIO.OUT)
GPIO.setup(CAM_ON_PIN, GPIO.OUT)
GPIO.setup(SERVO_1_PIN,GPIO.OUT)
GPIO.setup(SERVO_2_PIN, GPIO.OUT)
#PWM setting on the pins of the servo-controller
servo1 = GPIO.PWM(SERVO_1_PIN,50)
servo2 = GPIO.PWM(SERVO_2_PIN, 54)
#Starting the servo-controller
servo1.start(0)
servo2.start(0)
czujnik = Czujnik() #Assing an object to communicate with the sensor
thread
#Assigning and starting the sensor handling thread
x = threading.Thread(target=distance_thread, kwargs={ "servo1" : servo1,
"servo2" : servo2, "czujnik" : czujnik })
x.start()
print("start procedure")
#Designation of the initial state of control buttons. The initial state
marked with "False" means the low state of control buttons
keyDownPress = False
keyUpPress = False
keyRightPress = False
keyLeftPress = False

#Led for the control system. Led signals start and readiness of  control
system
GPIO.output(READY_PIN, GPIO.HIGH)
keyboard = Controller()
```

Python is available on almost every operating system [16]. The one used in this project is the Raspberry Pi OS distributed by Linux. Time, Sys, Rpi GIPO, OS, Threading, and Pynput keyboard are all virtual libraries used in the project. Mater program executes things like robot steering, control of the remote control, and maintenance system.

```
#Button status reading function
def getCharPressed(key):
    try:
        return key.char
    except:
        return ""
#Global variable assignment
def on_press(key):
    global keyDownPress
    global keyUpPress
    global keyRightPress
    global keyLeftPress
    global czujnik
    print("Key pressed: {0}".format(key))
    if key == Key.esc: #The program will be turned off when "esc" button is used
        servo1.stop()
        servo2.stop()
        GPIO.output(READY_PIN, GPIO.LOW)
        czujnik.stop = True
   GPIO.cleanup()
        sys.exit()
    elif key == Key.down: #servo-controller motion initialization
        if not keyDownPress:
            servo1.ChangeDutyCycle(6.5)
            keyDownPress = True
    elif key == Key.up: #servo-controller motion initialization
        if not keyUpPress:
            servo1.ChangeDutyCycle(9)
            keyUpPress = True
    elif key == Key.left: #servo-controller motion initialization
        if not keyLeftPress:
            servo2.ChangeDutyCycle(5)
            keyLeftPress = True
    elif key == Key.right: #servo-controller motion initialization
        if not keyRightPress:
            servo2.ChangeDutyCycle(10.5)
            keyRightPress = True
    elif getCharPressed(key) == 's': #presing the "s" button activates the camera
        print("Starting the camera")
        os.system("/home/pi/Videos/RPi_Cam_Web_Interface/start.sh")
        GPIO.output(CAM_ON_PIN, GPIO.HIGH)
   elif getCharPressed(key) == 'd': #presing the "d" button turn off the camera
        print("Turn off the camera")
        os.system("/home/pi/Videos/RPi_Cam_Web_Interface/stop.sh")
        GPIO.output(CAM_ON_PIN, GPIO.LOW)
elif getCharPressed(key) == 'f': #presing the "f" button activates the assist control
system
        GPIO.output(DISTANCE_LED_PIN, GPIO.HIGH)
        czujnik.distanceThreadRun = True
    elif getCharPressed(key) == 'g': #presing the "g" button turn off the assist con-
trol system
        GPIO.output(DISTANCE_LED_PIN, GPIO.LOW)
        czujnik.distanceThreadRun = False
#Low status reading functions for control buttons
def on_release(key):
    global keyDownPress
    global keyUpPress
    global keyRightPress
```

```
    print("Key released: {0}".format(key))
    if key == Key.up:
        keyUpPress = False
    if key == Key.down:
        keyDownPress = False
    if key == Key.right:
        keyRightPress = False
    if key == Key.left:
        keyLeftPress = False

#Idle state of servo-controllers
    if key == Key.up or key == Key.down:
        servo1.ChangeDutyCycle(7.5)
    if key == Key.left or key == Key.right:
        servo2.ChangeDutyCycle(7.5)


try:
    with Listener(on_press=on_press, on_release=on_release) as li-
stener:
        listener.join()
except:
    print("ERROR")
    GPIO.cleanup()
```

A program, which executes assist control system, is based on a 'distance-thread' library. It is fully responsible for supporting both the sensors, and reactions of servo-controller to any given obstacle. If the distance between the robot, and obstacle is less than 25 cm, the program sends impulses to the steering control mechanism. That causes wheels to turn in the opposite direction, from where the signal is coming.

```
#libraries used
from distance import Czujnik
import RPi.GPIO as GPIO
import time

#pins designation
GPIO_TRIGGER = 12
GPIO_ECHO = 18
GPIO_TRIGGER2 = 16
GPIO_ECHO2 = 22

#Pins initialization
def init():
    GPIO.setmode(GPIO.BOARD)
    GPIO.setup(GPIO_TRIGGER, GPIO.OUT)
    GPIO.setup(GPIO_ECHO, GPIO.IN)
    GPIO.setup(GPIO_TRIGGER2, GPIO.OUT)
    GPIO.setup(GPIO_ECHO2, GPIO.IN)
```

```
#Function for measuring the distance from sensors to obstacles
def distance(triggerPin, echoPin):
    GPIO.output(triggerPin, True)
    time.sleep(0.00001)
    GPIO.output(triggerPin, False)
    StartTime = time.time()
    StopTime = time.time()
    while GPIO.input(echoPin) == 0:
        StartTime = time.time()
    while GPIO.input(echoPin) == 1:
        StopTime = time.time()
    TimeElapsed = StopTime - StartTime
    distance = (TimeElapsed * 34300) / 2  #reference to the speed of li-
ght

return distance #return variable distance

#The function of handling sensors and the reaction of the steering servo-
controller to an obstacle
def distance_thread(servo1, servo2, czujnik):
    init()
    try:
        while not czujnik.stop: #The loop continues until interrupted by
the second script
            if not czujnik.distanceThreadRun:
                continue #In case of system shutdown, the program below
does not run
            time.sleep(0.01)
            dist = distance(GPIO_TRIGGER, GPIO_ECHO) #reading data from
sensor 1 (distance in cm)
            dist2 = distance(GPIO_TRIGGER2, GPIO_ECHO2) #reading data
from sensor 1 (distance in cm)
                print("obstacle 1")
                servo2.ChangeDutyCycle(10)
                time.sleep(1)
                servo2.ChangeDutyCycle(7.5)
            if dist2 < 25: #The condition will only be work if the di-
stance is less than 25 cm
                print("obstacle 2")
                servo2.ChangeDutyCycle(5)
                time.sleep(1)
                servo2.ChangeDutyCycle(7.5)
    except KeyboardInterrupt:
        print("Measurement stopped by User")
        GPIO.cleanup()
    print("Off system")
```

VISION SYSTEM

Vision system works through ArduCam OV5647 camera with sensor OV5647 (Fig. 6). The camera can zoom in, and set the focus, which is certainly an advantage when the robot is on the move. 5Mpx Image sensor supports 1080px/30fps. A camera module is equipped with lens LS-2718 CS with 4 mm focal length, 93degree

field of view, and 1.4 iris. That setup allows recording of the whole area in front of the robot.

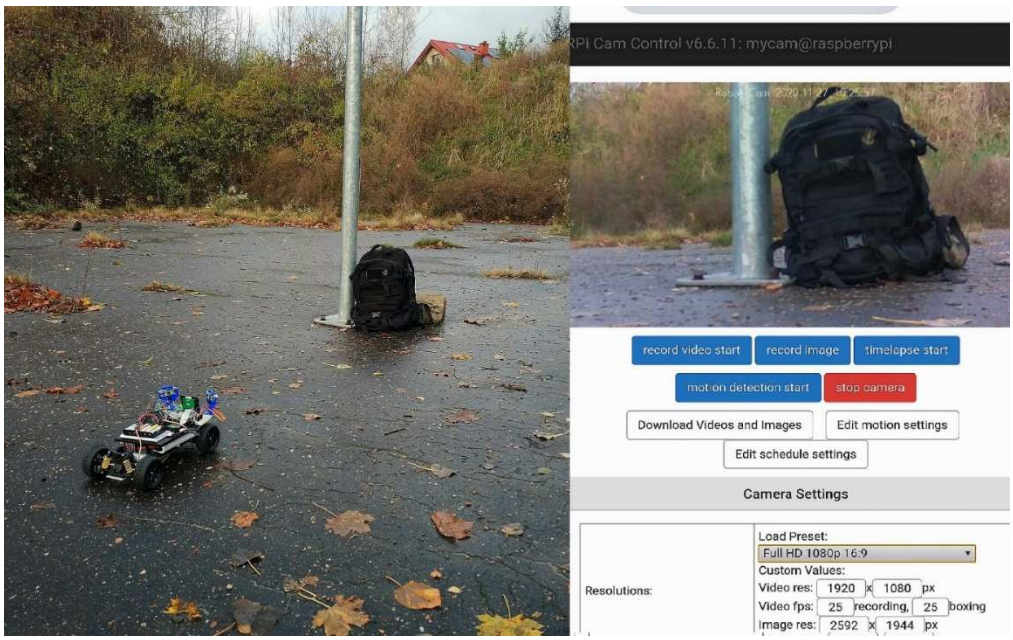

Fig. 7 Vision system - interface RPi Cam-Web

Realtime preview is possible through RPI-CAM-WEB (RPCWI) interface (Fig. 7). The expanded interface enables control of the settings of the camera through a browser script. RPCWI allows the user to record, and save all the data on the micro SD card, and then change every setting like saturation, or contrast. The camera interface is compatible with Linux. It shares a dedicated apache server that shows a preview of the camera view from all the mobile devices with any internet browser.

CONCLUSIONS

The presented vehicular mobile robot is good support for almost any of the alarm sub-unit. The mounted camera allows the user to spot, and identify any threats during the patrol. Because implementing universal software robot can be used for tasks inside the buildings where it can spot unidentified objects, or support the tasks of the soldiers inside the building. Future recourses will be focusing on enhancing the autonomous capabilities of the robot, as well as configuring the algorithms so multiple robots can operate more complex tasks

REFERENCES

[1] Eric Matthes, *Python Crash Course*, 2nd Edition: A Hands-On, Project-Based Introduction to Programming, Functions, 2019, pp.129-156

[2] Ignacy Dulęba. *Metody i algorytmy planowania ruchu robotów mobilnych i manipulacyjnych*

[3] Jung Hyun Choi, Kangwagye Samuel, Kanghyun Nam, Sehoon Oh, *An Autonomous Human Following Caddie Robot with High-Level Driving Functions*. Electronics 2020, *9*, 1516. https://doi.org/10.3390/electronics9091516

[4] Jurczyk Karolina, Piskur Paweł, Szymak Piotr, *Parameters Identification of the Flexible Fin Kinematics Model Using Vision and Genetic Algorithms*, Polish Maritime Research, *27*(2), 39-47, 2020, doi: https://doi.org/10.2478/pomr-2020-0025

[5] Lentin Joseph*, Nauka robotyki z językiem Python*, 2016

[6] Maciej Michałek, Dariusz Pazderski. *Sterowanie robotów mobilnych* : laboratorium, 2012

[7] Mariusz J. Giergiel, Zenon Hendzel, Wiesław Żylski. *Modelowanie i sterowanie mobilnych robotów kołowych,* PWN 2013

[8] Mark W. Spong, Seth Hutchinson, M. Vidyasagar, *Robot Modeling and Control*, 2nd Edition, 2020, pp. 365-373

[9] Matt Timmons-Brown, *Learn Robotics with Raspberry Pi: Build and Code Your Own Moving, Sensing, Thinking Robots*, 2019,

[10] Peter I. Corke, Robotics, *Vision and Control: Fundamental Algorithms in MATLAB*, 2nd ed. 2017 Edition

[11] Piotr Kulczycki, Józef Korbicz, Janusz Kacprzyk. *Automatyka, robotyka i przetwarzanie informacji*, PWN 2020

[12] Piotr Szymak, Pawel Piskur, Krzysztof Naus. (2020), *The Effectiveness of Using a Pretrained Deep Learning Neural Networks for Object Classification in Underwater Video, Remote Sensing*. 12.2020, doi: 10.3390/rs12183020.

[13] Piskur Pawel; Szymak Piotr; Jaskólski Krzysztof; Flis, Leszek; Gąsiorowski Marek, *Hydroacoustic System in a Biomimetic Underwater Vehicle to Avoid Collision with Vessels with Low-Speed Propellers in a Controlled Environment. Sensors*, 2020,

https://doi.org/10.3390/s20040968

[14] Przybylski Michał, Szymak Piotr, Kitowski Zygmunt, Piskur Pawel, *Comparison of Different Course Controllers of Biomimetic Underwater Vehicle with Two Tail Fins*. In: Bartoszewicz A., Kabziński J., Kacprzyk J. (eds) Advanced, Contemporary Control. Advances in Intelligent Systems and Computing, vol 1196. Springer, Cham., 2020,

https://doi.org/10.1007/978-3-030-50936-1_125

[15] Spyros G. Tzafestas, *Introduction to Mobile Robot Control, Mobile Robot Control V: Vision-Based Method,* 2014, pp. 319-351.

[16] Steven F. Lott *Python : programowanie funkcyjne*, 2019

[17] Wei Bin, *A Low Cost Introductory Platform for Advanced Robotic Control*. In: Venture G., Solis J., Takeda Y., Konno A. (eds) ROMANSY 23 - Robot Design, Dynamics and Control. ROMANSY 2020. CISM International Centre for Mechanical Sciences (Courses and Lectures), vol 601. Springer, Cham., 2020, https://doi.org/10.1007/978-3-030-58380-4_18

[18] Wiktor Hudy, Kazimierz Jaracz, *Laboratorium automatyki i robotyki*, 2013

[19] Wojciech Kaczmarek, Jarosław Panasiuk, Szymon Borys. *Środowiska programowania robotów*, PWN 2020

[20] www.electroschematics.com/wp-content/uploads/2013/07/HCSR04-datasheet-version-1.pdf

[21] www.piap.pl/produkt/roboty-mobilne-do-zastosowan-specjalnych/

[22] www.robotnik.eu/products/mobile-robots/summit-xl-hl/

MOBILNY ROBOT KOŁOWY DO WSPARCIA PODODDZIAŁU ALARMOWEGO

STRESZCZENIE

W artykule zaprezentowano mobilnego robota kołowego do wsparcia pododdziału alarmowego. Projekt został zrealizowany ze względu na rosnące potrzeby identyfikacji, kontroli oraz obserwacji. Cześć programistyczna została zaimplementowana w oparciu o minikomputer Raspberry Pi 4 B, z wykorzystaniem środowiska programistycznego PYTHON oraz dostępnych bibliotek. Cześć konstrukcyjna bazuje na szkielecie komponentowym zbudowanym na głównym elemencie podwoziowym. W projekcie wykorzystano kompatybilne czujniki uzupełniające funkcjonalność robota oraz kamerę z obiektywem, która wraz z zastosowanym interfejsem realizuje pogląd obrazu w czasie rzeczywistym.

Robot przeznaczony jest do eliminowania zagrożeń wynikających z zadań pododdziału alarmowego poprzez wizyjną analizę pola obserwacji, dodatkowo umożliwia nadzór żołnierzy przebywających w strefach izolacyjnych oraz identyfikacje nierozpoznanych obiektów.

Słowa kluczowe:

robot mobilny, raspberry pi, phyton, sterowanie robotem mobilnym

SCIENTIFIC JOURNAL OF POLISH NAVAL ACADEMY
2020 (LXI) 4 (223)

sciendo

DOI:10.2478/sjpna-2020-0016

AN OPERATIONAL CALCULUS MODEL WITH THE (m, n)-SYMMETRIC DIFFERENCE

Hubert Wysocki*

[*]Polish Naval Academy, Faculty of Mechanical and Electrical Engineering, Śmidowicza 69 Str., 81-127 Gdynia, Poland; e-mail: h.wysocki@amw.gdynia.pl; ORCID ID 0000-0003-4487-8555

ABSTRACT

The paper determines a non-classical Bittner operational calculus model, in which the derivative is understood as an (m, n)-symmetric difference $D_{m,n}\{x(k)\} := \{x(k+m) - x(k-n)\}$. By considering an operation $D_{m,n,b}\{x(k)\} := \{x(k+m) - b(k)x(k-n)\}$, the formulated model has been generalized.

Key words:

operational calculus, derivative, integrals, limit conditions, (m, n)-symmetric difference.

Research article

FOUNDATIONS OF THE NON-CLASSICAL BITTNER OPERATIONAL CALCULUS

The *Bittner operational calculus* [1–4] is referred to as a system

$$CO(L^0, L^1, S, T_q, s_q, Q), \tag{1}$$

where L^0 and L^1 are linear spaces (over the same field Γ of scalars) such that $L^1 \subset L^0$. The linear operation $S : L^1 \longrightarrow L^0$ (denoted as $S \in \mathscr{L}(L^1, L^0)$), called the (abstract) *derivative*, is a surjection. Moreover, Q is a set of indices q for the operations $T_q \in \mathscr{L}(L^0, L^1)$ such that $S\,T_q f = f, f \in L^0$, called *integrals* and for the operations $s_q \in \mathscr{L}(L^1, L^1)$ such that $s_q x = x - T_q S\,x, x \in L^1$, called *limit conditions*. The kernel of S, i.e. Ker S is called a set of *constants* for the derivative S.

It easy to verify that the limit conditions $s_q, q \in Q$ are projections of L^1 onto the subspace Ker S.

If we define the objects (1), then we have in mind a *representation,* or a *model* of the operational calculus. In particular, representations of the operational calculus (1) are *discrete* models in which the derivative S can be understood as:
an n^{th}*-order forward difference* [16]

$$\Delta_n x(k) := x(k+n) - x(k), \tag{2}$$

an n^{th}*-order backward difference* [15]

$$\nabla_n x(k) := x(k) - x(k-n) \tag{3}$$

or a $2n^{th}$*-order central difference* [17]

$$D_n x(k) := x(k+n) - x(k-n), \tag{4}$$

where n is a given natural number.

An (m, n)*-symmetric difference*[1]

$$D_{m,n} x(k) := x(k+m) - x(k-n), \tag{5}$$

where m, n are given non-negative integers such that $m^2 + n^2 > 0$, is a generalization of the operations (2)–(4).

In this paper, one shall determine such an operational calculus model, in which the operation (5) will be the derivative S. Next, based on this model, we shall develop a more general representation with a derivative

[1] This notion is related to the α, β-symmetric difference derivative considered in [5,6].

$$D_{m,n,b}x(k) := x(k+m) - b(k)x(k-n)^2. \tag{6}$$

Certain specific models related to (6) were considered in literature before: a model with a derivative

$$D_{1,0,b}x(k) = x(k+1) - b(k)x(k)$$

was constructed in [10], whereas a model with a derivative

$$D_{0,1,b}x(k) = x(k) - b(k)x(k-1)$$

was considered in [13].

For b being a constant sequence, representations of operational calculus with derivatives

$$D_{n,0,b}x(k) = x(k+n) - bx(k),$$
$$D_{0,n,b}x(k) = x(k) - bx(k-n),$$
$$D_{n,n,b}x(k) = x(k+n) - bx(k-n)$$

were discussed in [16], [15], [17].

(m, n)-SYMMETRIC DIFFERENCE MODEL

Let $\mathbb{Z}$ and $\mathbb{C}$ denote sets of integers and complexes, respectively. Moreover, let $C(\mathbb{Z}, \mathbb{C})$ be a linear space of two-sided complex sequences $x = \{x(k)\}_{k\in\mathbb{Z}}$ with a common sequences addition, and sequences multiplication by complex numbers. Further, let

$$\varepsilon_0, \varepsilon_1, \ldots, \varepsilon_{\nu-1} \tag{7}$$

be roots of unity of order $\nu := m + n$, i.e.

$$\varepsilon_j = \cos\frac{2j\pi}{\nu} + \mathrm{i}\,\sin\frac{2j\pi}{\nu}, \quad j \in \overline{0, \nu-1}\,^3,$$

where 'i' is the imaginary unit.

[2] The sequences multiplication in (6) means a usual coordinate-wise (Hadamard) multiplication.

[3] $\overline{0, \nu-1} := \{0, 1, \ldots, \nu-1\}$.

Using the following properties of the sequence (7):

$$\varepsilon_j^{k+\ell\nu} = \varepsilon_j^k, \quad j \in \overline{0, \nu-1}, \quad k, \ell \in \mathbb{Z},$$
$$\varepsilon_0^r + \varepsilon_1^r + \ldots + \varepsilon_{\nu-1}^r = 0, \quad r \neq \ell\nu, \nu > 1, \ell, r \in \mathbb{Z}$$

we shall prove the below

Theorem 1. *A system* (1)*, where* $x = \{x(k)\} \in L^0 = L^1 := C(\mathbb{Z}, \mathbb{C}), k_0 \equiv q \in Q := \mathbb{Z}$ *and*

$$S\,x := \{x(k+m) - x(k-n)\}^4 \tag{8}$$

$$T_{k_0} x := \begin{cases} -\dfrac{1}{\nu} \displaystyle\sum_{j=0}^{\nu-1} \sum_{i=k+n}^{k_0+n-1} \varepsilon_j^{k+n-i}\, x(i) & for \quad k < k_0 \\ 0 & for \quad k = k_0 \\ \dfrac{1}{\nu} \displaystyle\sum_{j=0}^{\nu-1} \sum_{i=k_0+n}^{k+n-1} \varepsilon_j^{k+n-i}\, x(i) & for \quad k > k_0 \end{cases}, \quad k \in \mathbb{Z}, \tag{9}$$

$$s_{k_0} x := \left\{ \frac{1}{\nu} \sum_{j=0}^{\nu-1} \sum_{i=k_0}^{k_0+\nu-1} \varepsilon_j^{k-i}\, x(i) \right\} \tag{10}$$

forms a discrete model of the Bittner operational calculus[5]*.*

Proof. Obviously, the operations (8)–(10) are linear. Let $\{y(k)\} := T_{k_0}\{x(k)\}$. Hence, for $k = k_0$ we obtain

$$S\,\{y(k)\}|_{k=k_0} = \{y(k_0+m) - y(k_0-n)\}$$

$$= \left\{ \frac{1}{\nu} \sum_{j=0}^{\nu-1} \sum_{i=k_0+n}^{k_0+\nu-1} \varepsilon_j^{k_0-i}\, x(i) + \frac{1}{\nu} \sum_{j=0}^{\nu-1} \sum_{i=k_0}^{k_0+n-1} \varepsilon_j^{k_0-i}\, x(i) \right\} = \left\{ \frac{1}{\nu} \sum_{j=0}^{\nu-1} \sum_{i=k_0}^{k_0+\nu-1} \varepsilon_j^{k_0-i}\, x(i) \right\}$$

$$= \left\{ x(k_0) + \frac{1}{\nu} \sum_{i=k_0+1}^{k_0+\nu-1} \left(\varepsilon_0^{k_0-i} + \varepsilon_1^{k_0-i} + \cdots + \varepsilon_{\nu-1}^{k_0-i} \right) x(i) \right\} = \{x(k)\}|_{k=k_0}.$$

For $k < k_0$ and $k + m = k_0$ (i.e. $k = k_0 - m$), we have in turn

[4] $\{x(k)\}$ means a symbol of the sequence x, i.e. $x = \{x(k)\}$, whereas $x(k)$ means the k^{th}-term of the sequence $\{x(k)\}$, where $k \in \mathbb{Z}$. This notation originates from J. Mikusiński [11].

[5] Due to the definition of T_{k_0}, we assume that $\sum_{i=k_0+n}^{k_0+n-1} x(i) := 0$.

$$S\{y(k)\} = \{y(k+m) - y(k-n)\} = \{y(k_0) - y(k_0-\nu)\}$$

$$= \left\{0 + \frac{1}{\nu}\sum_{j=0}^{\nu-1}\sum_{i=k_0-m}^{k_0+n-1}\varepsilon_j^{k_0-m-i}\,x(i)\right\}$$

$$= \left\{x(k_0-m) + \frac{1}{\nu}\sum_{i=k_0-m+1}^{k_0+n-1}\left(\varepsilon_0^{k_0-m-i} + \varepsilon_1^{k_0-m-i} + \cdots + \varepsilon_{\nu-1}^{k_0-m-i}\right)x(i)\right\} = \{x(k_0-m)\}.$$

Therefore,

$$S\{y(k)\} = \{x(k_0-m)\} \quad \text{that is} \quad S\{y(k)\} = \{x(k)\}.$$

For $k < k_0$ and $k+m < k_0$ (i.e. $k+\nu < k_0+n$), we get

$$S\{y(k)\} = \{y(k+m) - y(k-n)\}$$

$$= \left\{\frac{1}{\nu}\sum_{j=0}^{\nu-1}\sum_{i=k}^{k_0+n-1}\varepsilon_j^{k-i}\,x(i) - \frac{1}{\nu}\sum_{j=0}^{\nu-1}\sum_{i=k+\nu}^{k_0+n-1}\varepsilon_j^{k-i}\,x(i)\right\} = \left\{\frac{1}{\nu}\sum_{j=0}^{\nu-1}\sum_{i=k}^{k+\nu-1}\varepsilon_j^{k-i}\,x(i)\right\}$$

$$= \left\{x(k) + \frac{1}{\nu}\sum_{i=k+1}^{k+\nu-1}\left(\varepsilon_0^{k-i} + \varepsilon_1^{k-i} + \cdots + \varepsilon_{\nu-1}^{k-i}\right)x(i)\right\} = \{x(k)\}. \tag{11}$$

When $k > k_0$ and $k+m > k_0$ (i.e. $k+\nu > k_0+n$), we obtain in turn

$$S\{y(k)\} = \{y(k+m) - y(k-n)\}$$

$$= \left\{\frac{1}{\nu}\sum_{j=0}^{\nu-1}\sum_{i=k_0+n}^{k+\nu-1}\varepsilon_j^{k-i}\,x(i) + \frac{1}{\nu}\sum_{j=0}^{\nu-1}\sum_{i=k}^{k_0+n-1}\varepsilon_j^{k-i}\,x(i)\right\} = \left\{\frac{1}{\nu}\sum_{j=0}^{\nu-1}\sum_{i=k}^{k+\nu-1}\varepsilon_j^{k-i}\,x(i)\right\},$$

so, by analogy to (11), we have $S\{y(k)\} = \{x(k)\}$.

If $k > k_0$ and $k-n = k_0$ (i.e. $k+m = k_0+\nu$), then

$$S\{y(k)\} = \{y(k+m) - y(k-n)\} = \{y(k_0+\nu) - y(k_0)\}$$

$$= \left\{\frac{1}{\nu}\sum_{j=0}^{\nu-1}\sum_{i=k_0+n}^{k_0+\nu+n-1}\varepsilon_j^{k_0+n-i}\,x(i) - 0\right\}$$

$$= \left\{x(k_0+n) + \frac{1}{\nu}\sum_{i=k_0+n+1}^{k_0+\nu+n-1}\left(\varepsilon_0^{k_0+n-i} + \varepsilon_1^{k_0+n-i} + \cdots + \varepsilon_{2n-1}^{k_0+n-i}\right)x(i)\right\} = \{x(k_0+n)\},$$

that is $S\{y(k)\} = \{x(k)\}$.

For $k > k_0$ and $k-n > k_0$ (i.e. $k > k_0+n$), we have

$$S\{y(k)\} = \{y(k+m) - y(k-n)\}$$

$$= \left\{\frac{1}{\nu}\sum_{j=0}^{\nu-1}\sum_{i=k_0+n}^{k+\nu-1}\varepsilon_j^{k-i}\,x(i) - \frac{1}{\nu}\sum_{j=0}^{\nu-1}\sum_{i=k_0+n}^{k-1}\varepsilon_j^{k-i}\,x(i)\right\} = \left\{\frac{1}{\nu}\sum_{j=0}^{\nu-1}\sum_{i=k}^{k+\nu-1}\varepsilon_j^{k-i}\,x(i)\right\},$$

which, similarly to (11), also means that $S\{y(k)\} = \{x(k)\}$.
Now, if $k > k_0$ and $k - n < k_0$ (i.e. $k < k_0 + n$), then

$$S\{y(k)\} = \{y(k+m) - y(k-n)\}$$

$$= \left\{\frac{1}{\nu}\sum_{j=0}^{\nu-1}\sum_{i=k_0+n}^{k+\nu-1}\varepsilon_j^{k-i}\,x(i) + \frac{1}{\nu}\sum_{j=0}^{\nu-1}\sum_{i=k}^{k_0+n-1}\varepsilon_j^{k-i}\,x(i)\right\} = \left\{\frac{1}{\nu}\sum_{j=0}^{\nu-1}\sum_{i=k}^{k+\nu-1}\varepsilon_j^{k-i}\,x(i)\right\} = \{x(k)\}.$$

Finally, we can confirm that the property $S\,T_{k_0}x = x$ is fulfilled.

Let $\{f(k)\} := S\{x(k)\} = \{x(k+m) - x(k-n)\}$. Then, for $k < k_0$ we get

$$T_{k_0}S\{x(k)\} = T_{k_0}\{f(k)\} = \left\{-\frac{1}{\nu}\sum_{j=0}^{\nu-1}\sum_{i=k+n}^{k_0+n-1}\varepsilon_j^{k+n-i}\,f(i)\right\}$$

$$= \left\{\frac{1}{\nu}\sum_{j=0}^{\nu-1}\Big[\sum_{i=k+n}^{k_0+n-1}\varepsilon_j^{k+n-i}\,x(i-n) - \sum_{i=k+n}^{k_0+n-1}\varepsilon_j^{k+n-i}\,x(i+m)\Big]\right\}$$

$$= \left\{\frac{1}{\nu}\sum_{j=0}^{\nu-1}\Big[\sum_{i=k}^{k_0-1}\varepsilon_j^{k-i}\,x(i) - \sum_{i=k+\nu}^{k_0+\nu-1}\varepsilon_j^{k-i}\,x(i)\Big]\right\}$$

$$= \left\{\frac{1}{\nu}\sum_{j=0}^{\nu-1}\Big[\sum_{i=k}^{k_0-1}\varepsilon_j^{k-i}\,x(i) + \sum_{i=k_0}^{k+\nu-1}\varepsilon_j^{k-i}\,x(i) - \Big(\sum_{i=k_0}^{k+\nu-1}\varepsilon_j^{k-i}\,x(i) + \sum_{i=k+\nu}^{k_0+\nu-1}\varepsilon_j^{k-i}\,x(i)\Big)\Big]\right\}$$

$$= \left\{\frac{1}{\nu}\sum_{j=0}^{\nu-1}\sum_{i=k}^{k+\nu-1}\varepsilon_j^{k-i}\,x(i)\right\} - \left\{\frac{1}{\nu}\sum_{j=0}^{\nu-1}\sum_{i=k_0}^{k_0+\nu-1}\varepsilon_j^{k-i}\,x(i)\right\}.$$

Hence, on the basis of (11), we eventually obtain

$$T_{k_0}S\{x(k)\} = \{x(k)\} - \left\{\frac{1}{\nu}\sum_{j=0}^{\nu-1}\sum_{i=k_0}^{k_0+\nu-1}\varepsilon_j^{k-i}\,x(i)\right\} = \{x(k)\} - s_{k_0}\{x(k)\}.$$

Similarly, if $k > k_0$, then

$$T_{k_0}S\{x(k)\} = T_{k_0}\{f(k)\} = \left\{\frac{1}{\nu}\sum_{j=0}^{\nu-1}\sum_{i=k_0+n}^{k+n-1}\varepsilon_j^{k+n-i}\,f(i)\right\}$$

$$= \left\{\frac{1}{\nu}\sum_{j=0}^{\nu-1}\Big[\sum_{i=k_0+n}^{k+n-1}\varepsilon_j^{k+n-i}\,x(i+m) - \sum_{i=k_0+n}^{k+n-1}\varepsilon_j^{k+n-i}\,x(i-n)\Big]\right\}$$

$$= \left\{\frac{1}{\nu}\sum_{j=0}^{\nu-1}\Big[\sum_{i=k_0+\nu}^{k+\nu-1}\varepsilon_j^{k-i}\,x(i) - \sum_{i=k_0}^{k-1}\varepsilon_j^{k-i}\,x(i)\Big]\right\}$$

$$= \left\{\frac{1}{\nu}\sum_{j=0}^{\nu-1}\Big[\sum_{i=k}^{k_0+\nu-1}\varepsilon_j^{k-i}\,x(i) + \sum_{i=k_0+\nu}^{k+\nu-1}\varepsilon_j^{k-i}\,x(i) - \Big(\sum_{i=k_0}^{k-1}\varepsilon_j^{k-i}\,x(i) + \sum_{i=k}^{k_0+\nu-1}\varepsilon_j^{k-i}\,x(i)\Big)\Big]\right\}$$

$$= \left\{\frac{1}{\nu}\sum_{j=0}^{\nu-1}\sum_{i=k}^{k+\nu-1}\varepsilon_j^{k-i}\,x(i)\right\} - \left\{\frac{1}{\nu}\sum_{j=0}^{\nu-1}\sum_{i=k_0}^{k_0+\nu-1}\varepsilon_j^{k-i}\,x(i)\right\} = \{x(k)\} - s_{k_0}\{x(k)\}.$$

Therefore, the property $T_{k_0}S\,x = x - s_{k_0}x$ is also fulfilled. □

Since for $k \in \overline{k_0+1, k_0+\nu-1}$ we have

$$\sum_{i=k_0+n}^{k+n-1}\left(\varepsilon_0^{k+n-i} + \varepsilon_1^{k+n-i} + \cdots + \varepsilon_{\nu-1}^{k+n-i}\right) = 0,$$

then, from the definition (9) of the integrals T_{k_0}, we get the following

Corollary1. *If* $\{y(k)\} := T_{k_0}\{x(k)\}$, *then*

$$y(k) = 0 \quad \textit{for} \quad k \in \overline{k_0, k_0+\nu-1}.$$

Example 1. We will list terms of the sequence $\{y(k)\} := T_{k_0}\{x(k)\}$ for $k \in \overline{-17, 24}$ when $m = 3, n = 2$ and $k_0 = 4$. Using (9), we obtain[6]

[6] *Mathematica*® was used for all computations in this paper.

k	$y(k)$	k	$y(k)$
-17	$-x(-15) - x(-10) - x(-5) - x(0) - x(5)$	4	0
-16	$-x(-14) - x(-9) - x(-4) - x(1)$	5	0
-15	$-x(-13) - x(-8) - x(-3) - x(2)$	6	0
-14	$-x(-12) - x(-7) - x(-2) - x(3)$	7	0
-13	$-x(-11) - x(-6) - x(-1) - x(4)$	8	0
-12	$-x(-10) - x(-5) - x(0) - x(5)$	9	$x(6)$
-11	$-x(-9) - x(-4) - x(1)$	10	$x(7)$
-10	$-x(-8) - x(-3) - x(2)$	11	$x(8)$
-9	$-x(-7) - x(-2) - x(3)$	12	$x(9)$
-8	$-x(-6) - x(-1) - x(4)$	13	$x(10)$
-7	$-x(-5) - x(0) - x(5)$	14	$x(6) + x(11)$
-6	$-x(-4) - x(1)$	15	$x(7) + x(12)$
-5	$-x(-3) - x(2)$	16	$x(8) + x(13)$
-4	$-x(-2) - x(3)$	17	$x(9) + x(14)$
-3	$-x(-1) - x(4)$	18	$x(10) + x(15)$
-2	$-x(0) - x(5)$	19	$x(6) + x(11) + x(16)$
-1	$-x(1)$	20	$x(7) + x(12) + x(17)$
0	$-x(2)$	21	$x(8) + x(13) + x(18)$
1	$-x(3)$	22	$x(9) + x(14) + x(19)$
2	$-x(4)$	23	$x(10) + x(15) + x(20)$
3	$-x(5)$	24	$x(6) + x(11) + x(16) + x(21)$

□

Each sequence $c = \{c(k)\}$ that is a constant for the derivative (8) is a ν-periodic sequence. Therefore, from the definition (10) of limit conditions s_{k_0} there follows the below

Corollary 2. *The numbers* $x(k_0), x(k_0 + 1), \ldots, x(k_0 + \nu - 1)$ *form a cycle of the* ν*-periodic sequence* $\{c(k)\} = s_{k_0}\{x(k)\}$*, i.e.*

$$c(k) = c(k + \ell\nu) = x(k), \quad k \in \overline{k_0, k_0 + \nu - 1}, \ell \in \mathbb{Z}.$$

PARTICULAR CASES

From Theorem 1 follow difference representations of the Bittner operational calculus mentioned at the beginning of this paper. Namely, for $n = 0$ we obtain the model with the forward difference (2) described in [16]. When $m = n$, we get in turn the model with the central difference (4) constructed in [17]. In [15] there was presented a model, in which to the backward difference (3) there correspond the following limit conditions

$$s_{\nabla_n,k_0}\{x(k)\} = \left\{\frac{1}{n}\sum_{j=0}^{n-1}\sum_{i=k_0-n+1}^{k_0}\varepsilon_j^{k-i}\,x(i)\right\} \tag{12}$$

and integrals

$$T_{\nabla_n,k_0}\{x(k)\} = \begin{cases} -\dfrac{1}{n}\displaystyle\sum_{j=0}^{n-1}\sum_{i=k+1}^{k_0}\varepsilon_j^{k-i}\,x(i) & \text{for} \quad k < k_0 \\ 0 & \text{for} \quad k = k_0 \\ \dfrac{1}{n}\displaystyle\sum_{j=0}^{n-1}\sum_{i=k_0+1}^{k}\varepsilon_j^{k-i}\,x(i) & \text{for} \quad k > k_0 \end{cases}, \quad k \in \mathbb{Z}. \tag{13}$$

This model is different to the one obtained from Theorem 1 for $m = 0$. The limit conditions (10) are uniquely determined by the initial conditions

$$x(k_0), x(k_0+1), \ldots, x(k_0+n-1),$$

while the limit conditions (12) depend on

$$x(k_0-n+1), x(k_0-n+2), \ldots, x(k_0).$$

Hence, the integrals (9) and (13) are also different, so

$$T_{k_0}T_{\nabla_n,k_0} \neq T_{\nabla_n,k_0}T_{k_0}.$$

GENERALIZATIONS

Let us consider the following generalization of the symmetric difference (8):

$$S_b\{x(k)\} := \{x(k+m) - b(k)x(k-n)\}, \tag{14}$$

where $b := \{b(k)\}$ is a real sequence satisfying the condition

$$\bigwedge_{k\in\mathbb{Z}} b(k) > 0.$$

In the spirit of the method described in [18], we shall define the integrals T_{b,k_0} and the limit conditions s_{b,k_0} corresponding to the derivative (14), called an (m,n)-*symmetric difference with the base* $b = \{b(k)\}$. In order to do this, we shall also use the following auxiliary theorems:

Lemma 1 (Th. 3 [4]). *An abstract differential equation*

$$S\,x = f, \quad f \in L^0, x \in L^1$$

with a limit condition

$$s_q x = x_{0,q}, \quad x_{0,q} \in \operatorname{Ker} S$$

has exactly one solution

$$x = x_{0,q} + T_q f.$$

Lemma 2 (Th. 4 [4]). *With the given derivative $S \in \mathscr{L}(L^1, L^0)$, the projection $s_q \in \mathscr{L}(L^1, \operatorname{Ker} S)$ determines an integral $T_q \in \mathscr{L}(L^0, L^1)$ from the condition*

$$x = T_q f \quad \textit{if and only if} \quad S\,x = f, s_q x = 0.$$

Moreover, the projection s_q is a limit condition corresponding to the integral T_q.

First, we will determine a positive sequence $d = \{d(k)\}$ such that $d \in \operatorname{Ker} S_b$ and

$$d(0) = d(1) = \ldots = d(\nu - 1) = 1.$$

Thus, we have

$$\ln(d(k+m)) - \ln(d(k-n)) = \ln(b(k)), \quad k \in \mathbb{Z},$$

so

$$h(k+m) - h(k-n) = u(k), \quad k \in \mathbb{Z} \tag{15}$$

and

$$h(0) = h(1) = \ldots = h(\nu - 1) = 0, \tag{16}$$

where

$$h = \{h(k)\} := \{\ln(d(k))\}, \quad u = \{u(k)\} := \{\ln(b(k))\}.$$

The initial value problem (15), (16) can be presented in the form of

$$S\,h = u, \quad s_0 h = 0,$$

where S is the symmetric difference (8), whereas s_0 is the limit condition (10) for $k_0 := 0$. A solution to this problem, based on Lemma 1, is of the following form:

$$h = T_0 u,$$

where T_0 is the integral (9) for $k_0 := 0$.

Finally, the sequence

$$d = \exp(T_0 u) \tag{17}$$

is the desired constant for the derivative (14), i.e.

$$d(k+m) = b(k)d(k-n), \quad k \in \mathbb{Z}.$$

Example 2. If b is a constant sequence and $m := 2, n := 1$ or $m := 1, n := 2$, then from (17) we obtain

$$\{d(k)\}=\{\ldots, b^{-3}, b^{-3}, b^{-3}, b^{-2}, b^{-2}, b^{-2}, b^{-1}, b^{-1}, b^{-1}, \underset{k=0}{1}, 1, 1, b, b, b, b^2, b^2, b^2, b^3, b^3, b^3, \ldots\}.$$

Generally, we have

$$d(k) = b^{\lfloor k/\nu \rfloor}, \quad k \in \mathbb{Z}^{7}. \qquad \square$$

Let us consider a difference equation

$$S_b\{x(k)\} = \{f(k)\},$$

i.e.

$$x(k+m) - b(k)x(k-n) = f(k), \quad k \in \mathbb{Z}. \tag{18}$$

Hence, we have

$$\frac{x(k+m)}{d(k+m)} - \frac{x(k-n)}{d(k-n)} = \frac{f(k)}{d(k+m)}, \quad k \in \mathbb{Z},$$

so

$$y(k+m) - y(k-n) = g(k), \quad k \in \mathbb{Z}, \tag{19}$$

where

$$y(k) := \frac{x(k)}{d(k)}, \quad g(k) := \frac{f(k)}{d(k+m)}, \quad k \in \mathbb{Z}. \tag{20}$$

The equation (19) can be presented in the form of

$$S\{y(k)\} = \{g(k)\}, \tag{21}$$

where $S \equiv D_{m,n}$ is the operation (8).

From Lemma 1 it follows that the below sequence

$$\{y(k)\} = s_{k_0}\{y(k)\} + T_{k_0}\{g(k)\},$$

where T_{k_0} and s_{k_0} are operations (9) and (10), is the solution to (21).

[7] $\lfloor r \rfloor$ means the floor (the integer part) of a real number r.

From (20) we obtain $x(k) = d(k)y(k), k \in \mathbb{Z}$. Finally,

$$\{x(k)\} = \{d(k)\}s_{k_0}\left\{\frac{x(k)}{d(k)}\right\} + \{d(k)\}T_{k_0}\left\{\frac{f(k)}{d(k+m)}\right\} \tag{22}$$

is the solution to (18).

If we assume that

$$\{\widetilde{c}(k)\} := s_{k_0}\left\{\frac{x(k)}{d(k)}\right\},$$

then $\{\widetilde{c}(k)\} \in \operatorname{Ker} S$, so

$$\widetilde{c}(k+m) = \widetilde{c}(k-n), \quad k \in \mathbb{Z}.$$

Let

$$s_{b,k_0}\{x(k)\} := \{d(k)\}s_{k_0}\left\{\frac{x(k)}{d(k)}\right\}, \quad k_0 \in Q := \mathbb{Z}, \{x(k)\} \in L^1. \tag{23}$$

Thus, for each $k \in \mathbb{Z}$ we get

$$\begin{aligned} S_b s_{b,k_0} x(k) &= d(k+m)\widetilde{c}(k+m) - b(k)d(k-n)\widetilde{c}(k-n) \\ &= d(k+m)(\widetilde{c}(k+m) - \widetilde{c}(k-n)) = d(k+m)\cdot 0 = 0, \end{aligned}$$

that is $s_{b,k_0} \in \mathscr{L}(L^1, \operatorname{Ker} S_b)$. Moreover, since $s_{k_0}\{\widetilde{c}(k)\} = \{\widetilde{c}(k)\}$, for each $k \in \mathbb{Z}$ we have

$$\begin{aligned} s_{b,k_0}^2 x(k) &= s_{b,k_0}[d(k)\widetilde{c}(k)] = e(k)s_{k_0}\left[\frac{d(k)\widetilde{c}(k)}{d(k)}\right] \\ &= d(k)s_{k_0}\widetilde{c}(k) = d(k)\widetilde{c}(k) = s_{b,k_0}x(k). \end{aligned}$$

Eventually, s_{b,k_0} is a projection of L^1 onto $\operatorname{Ker} S_b$ for each $k_0 \in \mathbb{Z}$. From Lemma 2 it follows that the projection s_{b,k_0} determines an *integral* T_{b,k_0} from (22). Namely,

$$T_{b,k_0}\{f(k)\} := \{d(k)\}T_{k_0}\left\{\frac{f(k)}{d(k+m)}\right\}, \quad k_0 \in Q, \{f(k)\} \in L^0. \tag{24}$$

What is more, s_{b,k_0} is a *limit condition* corresponding to the integral (24).

Finally, we arrive at the

Corollary 3. *The system* (14), (23), (24) *forms a discrete model of the Bittner operational calculus.*

Example 3. Let us consider an initial value problem

$$x(k+1) - e^k x(k-2) = 0, \quad k \in \mathbb{Z} \tag{25}$$

$$x(0) = 3, x(1) = x(2) = 0. \tag{26}$$

The homogeneous equation (25) takes the form of $S_b x = 0$, where S_b is the forward difference (14) for $m := 1, n := 2, b := \{e^k\}$. From (22) we get the solution to (25) expressed by the limit condition (23), i.e.

$$\{x(k)\} = s_{\{e^k\},0}\{x(k)\} = \{d(k)\}s_0\left\{\frac{x(k)}{d(k)}\right\},$$

which depends of the sequence

$$\{d(k)\} = \exp(T_0\{k\})$$

and initial conditions (26).

Therefore,

$$x(k) = \begin{cases} \left(1 + 2\cos\left(\frac{2k\pi}{3}\right)\right)\exp\left(-\frac{1}{3}\sum\limits_{j=0}^{2}\sum\limits_{i=k+2}^{1} i\,\varepsilon_j^{k+2-i}\right) & \text{for} \quad k < 0 \\ \left(1 + 2\cos\left(\frac{2k\pi}{3}\right)\right)\exp\left(\frac{1}{3}\sum\limits_{j=0}^{2}\sum\limits_{i=2}^{k+1} i\,\varepsilon_j^{k+2-i}\right) & \text{for} \quad k \geqslant 0 \end{cases}, \quad k \in \mathbb{Z}, \text{ (27)}$$

i.e.

$$\{x(k)\} = \{\ldots, 0, 0, 3e^{12}, 0, 0, 3e^5, 0, 0, 3e, 0, 0, \underset{k=0}{3}, 0, 0, 3e^2, 0, 0, 3e^7, 0, 0, 3e^{15}, 0, 0, \ldots\}.$$

□

Example 4. Referring to the previous example, let us consider the Cauchy problem

$$x(k+1) - e^k x(k-2) = 1, \quad k \in \mathbb{Z} \tag{28}$$

$$x(0) = 3, x(1) = x(2) = 0. \tag{29}$$

From (24) and (22) it follows that the sequence

$$\{x(k)\} = T_{\{e^k\},0}\{1\} = \{d(k)\}T_0\left\{\frac{1}{d(k+1)}\right\}$$

is a solution to the nonhomogeneous equation (28) with the conditions $x(0) = x(1) = x(2) = 0$. Thus,

$$x(k) = \begin{cases} -\frac{1}{3}\exp\left(-\frac{1}{3}\sum\limits_{j=0}^{2}\sum\limits_{i=k+2}^{1} i\,\varepsilon_j^{k+2-i}\right)\sum\limits_{j=0}^{2}\sum\limits_{i=k+2}^{1}\exp\left(-\frac{1}{2}(i+1)(i+4)\right)\varepsilon_j^{k+2-i} & \text{for} \quad k < 0 \\ \frac{1}{3}\exp\left(\frac{1}{3}\sum\limits_{j=0}^{2}\sum\limits_{i=2}^{k+1} i\,\varepsilon_j^{k+2-i}\right)\sum\limits_{j=0}^{2}\sum\limits_{i=2}^{k+1}\exp\left(-\frac{1}{2}(i+1)(i+4)\right)\varepsilon_j^{k+2-i} & \text{for} \quad k \geqslant 0 \end{cases},$$

$$k \in \mathbb{Z}. \text{ (30)}$$

Eventually, basing on (22), the sum of the sequences (27) and (30) is a solution to the problem (28),(29), the values of which (for $k \in \overline{-17, 16}$) are presented in the table below:

k	$x(k)$	k	$x(k)$
-17	$-e^{15}-e^{27}-e^{36}-e^{42}-2e^{45}$	0	3
-16	$-e^{14}-e^{25}-e^{33}-e^{38}-e^{39}-e^{40}$	1	0
-15	$-e^{13}-e^{23}-e^{30}-e^{34}-2e^{35}$	2	0
-14	$-e^{12}-e^{21}-e^{27}-2e^{30}$	3	$1+3e^{2}$
-13	$-e^{11}-e^{19}-e^{24}-e^{25}-e^{26}$	4	1
-12	$-e^{10}-e^{17}-e^{21}-2e^{22}$	5	1
-11	$-e^{9}-e^{15}-2e^{18}$	6	$1+e^{5}+3e^{7}$
-10	$-e^{8}-e^{13}-e^{14}-e^{15}$	7	$1+e^{6}$
-9	$-e^{7}-e^{11}-2e^{12}$	8	$1+e^{7}$
-8	$-e^{6}-2e^{9}$	9	$1+e^{8}+e^{13}+3e^{15}$
-7	$-e^{5}-e^{6}-e^{7}$	10	$1+e^{9}+e^{15}$
-6	$-e^{4}+2e^{5}$	11	$1+e^{10}+e^{17}$
-5	$-2e^{3}$	12	$1+e^{11}+e^{19}+e^{24}+3e^{26}$
-4	$-e-e^{2}$	13	$1+e^{12}+e^{21}+e^{27}$
-3	$2e$	14	$1+e^{13}+e^{23}+e^{30}$
-2	-1	15	$1+e^{14}+e^{25}+e^{33}+e^{38}+3e^{40}$
-1	$-e^{-1}$	16	$1+e^{15}+e^{27}+e^{36}+e^{42}$

□

Basing on Theorem 1, it is not difficult to determine the integrals T_{a,b,k_0} and the limit conditions s_{a,b,k_0} corresponding to an (m,n)-*symmetric difference* with the bases $a=\{a(k)\}, b=\{b(k)\}$:

$$S_{a,b}\{x(k)\} := \{a(k)x(k+m)-b(k)x(k-n)\}, \tag{31}$$

where

$$\bigwedge_{k\in\mathbb{Z}} a(k)b(k)>0 \quad \text{(cf. [14])}.$$

Namely, by representing the derivative (31) in the form of

$$S_{a,b}\{x(k)\} = \{a(k)\}\left\{x(k+m)-\frac{b(k)}{a(k)}x(k-n)\right\} = \{a(k)\}S_{b/a}\{x(k\},$$

we obtain

$$T_{a,b,k_0}\{x(k)\} = T_{b/a,k_0}\left\{\frac{x(k)}{a(k)}\right\}, \qquad s_{a,b,k_0}\{x(k)\} = s_{b/a,k_0}\{x(k)\},$$

where $S_{b/a}$ and $T_{b/a,k_0}$, $s_{b/a,k_0}$ are operations (14),(24),(23), in which the sequence b needs to be replaced with the sequence b/a.

REFERENCES

[1] Bittner R., *On certain axiomatics for the operational calculus*, 'Bull. Acad. Polon. Sci.', Cl. III, 1959, 7(1), pp. 1-9.

[2] Bittner R., *Operational calculus in linear spaces*, 'Studia Math.', 1961, 20, pp. 1–18.

[3] Bittner R., *Algebraic and analytic properties of solutions of abstract differential equations*, 'Rozprawy Matematyczne' ['Dissertationes Math.'], 42, PWN, Warszawa 1964.

[4] Bittner R., *Rachunek operatorów w przestrzeniach liniowych*, PWN, Warszawa 1974 [*Operational Calculus in Linear Spaces* — available in Polish].

[5] Brito da Cruz A. M. C., *Symmetric Quantum Calculus,* PHD thesis, University of Aveiro, Department of Mathematics, 2012 [online], https://arxiv.org/pdf/1306.1327 [access 29.12.2020].

[6] Brito da Cruz A. M. C., Martins N., Torres D. F. M., A *Symmetric Quantum Calculus*, In: Pinelas S., Chipot M., Dosla Z. (eds), 'Differential and Difference Equations with Applications', Springer Proceedings in Mathematics & Statistics, vol. 47, pp. 359-366. Springer, New York 2013 [online], https://arxiv.org/pdf/1112.6133 [access 29.12.2020]

[7] Elaydi S., *An Introduction to Difference Equations*, Springer Sci. and Business Media, New York 2005.

[8] Levy H., Lessman F., *Finite Difference Equations*, Pitman & Sons, London 1959.

[9] Mickens R. E., *Difference Equations: Theory, Applications and Advanced* Topics, Chapman & Hall/CRC Press, Boca Raton 2005.

[10] Mieloszyk E., *Example of operational calculus,* 'Zeszyty Naukowe Politechniki Gdańskiej, Matematyka XIII', 1985, 383, pp. 151-157.

[11] Mikusiński J., *Operational Calculus*, Pergamon Press 1959.

[12] Spiegel M. R., *Schaum*'s *Outline of Calculus of Finite Differences and Difference Equations*, McGraw-Hill, New York 1971.

[13] Wysocki H., *The nabla difference model of the operational calculus*, 'Demonstratio Math.', 2013, Vol. 46, No. 2, pp. 315-326.

[14] Wysocki H., *Model rachunku operatorów dla różnicy wstecznej przy podstawach a, b,* 'Zeszyty Naukowe Akademii Marynarki Wojennej', 2013, 1(192), pp. 109-120 [*The backward a, b-difference operational calculus model* – available in Polish].

[15] Wysocki H., *The operational calculus model for the n^{th}-order backward difference*, 'Zeszyty Naukowe Akademii Marynarki Wojennej — Scientific Journal of PNA', 2015, 3(202), pp. 75–88.

[16] Wysocki H., *An operational calculus model for the n^{th}-order forward difference*, 'Zeszyty Naukowe Akademii Marynarki Wojennej — Scientific Journal of PNA', 2017, 3(210), pp. 107–117.

[17] Wysocki H., *An operational calculus model for the central difference and exponential-trigonometric and hyperbolic Fibonacci sequences*, 'Scientific Journal of Polish Naval Academy — Zeszyty Naukowe AMW', 2018, 3(214), pp. 39-62.

[18] Wysocki H., *A generalization of difference models of the Bittner operational calculus*, 'Scientific Journal of Polish Naval Academy', 2019, 4(219), pp. 41-52.

MODEL RACHUNKU OPERATORÓW Z RÓŻNICĄ (m, n)-SYMETRYCZNĄ

STRESZCZENIE

W pracy określono model dyskretny nieklasycznego rachunku operatorów Bittnera, w którym pochodna rozumiana jest jako różnica (m, n)-symetryczna $D_{m,n}\{x(k)\} := \{x(k+m) - x(k-n)\}$. Dokonano uogólnienia opracowanego modelu rozważając operację $D_{m,n,b}\{x(k)\} := \{x(k+m) - b(k)x(k-n)\}$.

Słowa kluczowe:
rachunek operatorów, pochodna, pierwotne, warunki graniczne, różnica (m, n)-symetryczna.

RECENZENCI WYDAŃ W 2020 ROKU
REVIEWERS FOR 2020 ISSUES

Dr hab. inż. st. of. Jarosław Artyszuk, prof. AMS
Dr hab. inż. Elżbieta Bogalecka, Politechnika Gdańska
Dr inż. Wiesław Citko, Uniwersytet Morski w Gdyni
Dr hab. inż. Mirosław Czechowski, prof. UMG
Assistant Prof. Mohamed Elsaied, PhD, National Institute of Oceanography and Fisheries in Egypt
Prof. dr hab. inż Mariusz Giergiel, Akademia Górniczo-Hutnicza
Prof. dr hab. inż. Marek Grzegorzewski, Lotnicza Akademia Wojskowa w Dęblinie
Dr hab. inż. Maciej Gucma, Akademia Morska w Szczecinie
Prof. dr hab. inż. Marek Hartman, Uniwersytet Morski w Gdyni
Dr hab. inż. Piotr Jankowski, Uniwersytet Morski w Gdyni
Dr hab. inż. Lech Kasyk, prof. AMS, Akademia Morska w Szczecinie
Prof. dr hab. inż. Ryszard Katulski, Politechnika Gdańska
Prof. dr hab. Krzysztof Kołowrocki, Uniwersytet Morski w Gdyni
Prof. dr hab. inż. Zbigniew Korczewski, Politechnika Gdańska
Dr hab. inż. Izabela Krzysztofik, Politechnika Świętokrzyska
Dr inż. Karol Listewnik, Uniwersytet Morski w Gdyni
Dr hab. inż. Edyta Ładyżyńska-Kozdraś, prof. PW, Politechnika Warszawska
Dr hab. inż. Jarosław Markowski, Politechnika Poznańska
Prof. dr hab. inż. Eligiusz Mieloszyk, Politechnika Gdańska
Prof. dr hab. inż. Janusz Narkiewicz, Politechnika Warszawska
Dr hab. Hoang Nguyen, prof. UMG
Dr hab. inż. Juliusz Orlikowski, Politechnika Gdańska
Prof. dr hab. inż. Ireneusz Pielecha, Politechnika Poznańska
Prof. dr hab. Krystian Pyka, Akademia Górniczo-Hutnicza
Dr hab. Joanna Soszyńska-Budny, prof. UMG
Prof. dr hab. Andrzej Stateczny, Politechnika Gdańska
Dr hab. inż Tadeusz Stupak, prof. UMG
Dr hab. Cezary Szczepański, prof. PW, Politechnika Wrocławska
Dr hab. inż. Piotr Szymak, Akademia Marynarki Wojennej
Dr hab. inż. Santina Topolska, Politechnika Śląska
Prof. dr hab. inż. Maciej Walkowiak, Uniwersytet Technologiczno-Przyrodniczy w Bydgoszczy
Dr inż. Mirosław Włas, Politechnika Gdańska
Prof. dr hab. inż. Józef Żurek, Instytut Techniczny Wojsk Lotniczych

INFORMATION FOR AUTHORS

1. All submissions should be in the Microsoft Word word processor (.doc or .docx). They should not be longer than one author's sheet. Since 2015 English has been used as the language for publications in 'Scientific Journal of Polish Naval Academy' and the editorial boards admits papers written in English exclusively. All papers are reviewed.

   The reviewing procedures

   The reviewing procedure complies with the recommendations of the Ministry of Science and Higher Education. Editors (knowledgeable and qualified in the field of study) make initial assessment if paper submitted to the editor's office are suitable to the journal and if review is warranted. Afterwards the papers are reviewed by two independent reviewers. They hold the title of professor or a post-doctoral degree in the specific field and they have a reputation of fair and unbiased reviewers. The journal uses the double-blind review process. If the selected reviewer does not accept the proposal to performing a review, the Editorial Board of SJ of PNA may select another reviewer. In cases of controversy, additional reviewers are appointed. Assessments of all reviewers are treated with due respect. The review is in writing and concludes with an unequivocal recommendation to accept the paper for publication or to reject it. The reviewers are not allowed to use their knowledge about the paper prior to its publication. The author is notified of the result of the review process and is provided access to the review once the reviewer's identity has been blinded. Afterwards correspondence with the Editorial Board SJ PNA concerned with eventual comments becomes possible. The list of reviewers is announced once a year.

    Authors are required to submit the paper together with the declaration of contribution to the paper submitted (available at the website of the Polish Naval Academy: Science → Scientific journals → Scientific Journal of Polish Naval Academy → Informacje dla Autorów. Information for Authors).

2. Paper layout:
   - title
   - first name and last name (surname)
   - detailed affiliation
   - abstract
   - key words
   - introduction
   - main body including research methodology and obtained results
   - conclusions (or summary)
   - list of references
   - title, abstract and key words in the Polish language.
3. Numbered figures and tables.
4. Formulas:
   - numbered
   - written in a formula editor.
5. List of references:
   - in the alphabetical order
   - written in ISO 690 format.

INFORMACJE DLA AUTORÓW

1. Artykuł należy dostarczyć w wersji elektronicznej w formacie edytora Word (.doc lub .docx).

   Nie powinna przekraczać objętości jednego arkusza autorskiego. Od 2015 roku językiem publikacji w „Scientific Journal of Polish Naval Academy" jest język angielski; redakcja SJ PNA przyjmuje artykuły wyłącznie w tym języku. Wszystkie artykuły są recenzowane.

   Przebieg procedury recenzowania

   Procedura recenzowania artykułów jest zgodna z zaleceniami Ministerstwa Nauki i Szkolnictwa Wyższego. Artykuły złożone w Redakcji SJ PNA są poddawane ocenie formalnej przez redaktorów tematycznych, kwalifikowane do recenzji merytorycznych, a następnie recenzowane przez dwóch niezależnych recenzentów, którymi są osoby mające tytuł naukowy profesora lub stopień naukowy doktora habilitowanego w danej dziedzinie i reputację rzetelnego recenzenta. Recenzowanie odbywa się w systemie *double-blind review process.* Jeżeli recenzent nie podejmuje się wykonania recenzji, Komitet Redakcyjny SJ PNA może wyznaczyć innego recenzenta. W przypadkach spornych powoływani są dodatkowi recenzenci. Opinie wszystkich recenzentów są należycie respektowane. Recenzja ma formę pisemną i kończy się jednoznacznym wnioskiem co do dopuszczenia artykułu do publikacji lub jego odrzucenia. Recenzentom nie wolno wykorzystywać wiedzy na temat artykułu przed jego publikacją. Autor jest informowany o wyniku recenzji i otrzymuje ją do wglądu po zatajeniu nazwiska recenzenta, następnie jest możliwa korespondencja z Redakcją SJ PNA, dotycząca ewentualnych uwag. Raz w roku podawana jest lista recenzentów.

   Artykuły są publikowane na licencji CC BY-NC-ND 4.0. Autorzy są zobowiązani do złożenia artykułu wraz z oświadczeniem o wkładzie w powstanie publikacji (dostępne na stronie internetowej AMW w zakładce Nauka → Czasopisma naukowe → Scientific Journal of Polish Naval Academy → Informacje dla Autorów. Information for Authors).

2. Układ artykułu:
   - tytuł
   - imię i nazwisko
   - szczegółowa afiliacja
   - streszczenie
   - słowa kluczowe
   - wstęp
   - część zasadnicza opisująca metodykę badań i uzyskane wyniki
   - wnioski (lub podsumowanie)
   - bibliografia
   - tytuł, streszczenie i słowa kluczowe w języku polskim.
3. Rysunki i tabele ponumerowane.
4. Wzory:
   - ponumerowane
   - pisane w edytorze równań.
5. Bibliografia:
   - uporządkowana alfabetycznie
   - zapisana w formacie ISO 690.